Nano Research

ISSN 1998-0124 CN 11-5974/O4
https://doi.org/10.26599/NR.2026.94909282

Research Article

Magnetic-field-induced micro-potential promotes charge separation in S-vacancy-rich ZIS/MoS_2/Mo heterostructure for efficient photocatalytic H_2 evolution

Chao Cui[1](✉), Bei Li[2], Liwei Zhu[1], Wencai Zhu[1], Xiaolei Zhao[3], Xiaoning Wang[4], Yuanhua Sang[2], Hong Liu[2], Yan Zhang[1](✉), Zhaoke Zheng[2](✉)

[1] School of Chemistry and Chemical Engineering, Shandong Provincial Engineering Research Center for Anti-aging Cosmetics, Qilu Normal University, Jinan 250200, China

[2] State Key Laboratory of Crystal Materials, Shandong University, Jinan 250100, China

[3] School of Chemistry and Chemical Engineering, Taishan University, Taian 271000, China

[4] School of Transportation and Civil Engineering, Shandong Jiaotong University, Jinan 250357, China

Nano Res., **Just Accepted Manuscript** • https://doi.org/10.26599/NR.2026.94909282

https://www.sciopen.com/journal/1998-0124 on Oct. 25, 2026

© The Authors(s)

Just Accepted

This is a "Just Accepted" manuscript, which has been examined by the peer-review process and has been accepted for publication. A "Just Accepted" manuscript is published online shortly after its acceptance,which is prior to technical editing and formatting and author proofing. Tsinghua University Press (TUP) provides "Just Accepted" as an optional and free service which allows authors to make their results available to the research community as soon as possible after acceptance. After a manuscript has been technically edited and formatted, and the page proofs have been corrected, it will be removed from the "Just Accepted" web site and published officially with volume and article number (e.g., *Nano Research*, **2025**, *18*, 94906990). Please note that technical editing may introduce minor changes to the manuscript text and/or graphics which may affect the content, and all legal disclaimers that apply to the journal pertain. In no event shall TUP be held responsible for errors or consequences arising from the use of any information contained in these "Just Accepted" manuscripts. To cite this anuscript please use its Digital Object Identifier (DOI®),which is identical for all formats of publication.

Research Article

Magnetic-field-induced micro-potential promotes charge separation in S-vacancy-rich ZIS/MoS_2/Mo heterostructure for efficient photocatalytic H_2 evolution

Chao Cui[1,✉], Bei Li[2], Liwei Zhu[1], Wencai Zhu[1], Xiaolei Zhao[3], Xiaoning Wang[4], Yuanhua Sang[2], Hong Liu[2], Yan Zhang[1,✉], and Zhaoke Zheng[2,✉]

[1] *School of Chemistry and Chemical Engineering, Shandong Provincial Engineering Research Center for Anti-aging Cosmetics, Qilu Normal University, Jinan 250200, China*

[2] *State Key Laboratory of Crystal Materials, Shandong University, Jinan 250100, China*

[3] *School of Chemistry and Chemical Engineering, Taishan University, Taian 271000, China*

[4] *School of Transportation and Civil Engineering, Shandong Jiaotong University, Jinan 250357, China*

Received: 12 August 2026; **Revised:** 19 October 2026; **Accepted:** 25 October 2026

✉Address correspondence to Chao Cui, chaocui_sdu@163.com; Yan Zhang, yanzhang_2003@163.com; Zhaoke Zheng, zkzheng@sdu.edu.cn

Cite this article: *Nano Research*, 2026, 19, 94909282 https://doi.org/10.26599/NR.2026.94909282

Just Accepted

ABSTRACT: Enhancing charge separation in the absence of external bias remains a central challenge in photocatalytic hydrogen evolution. Herein, a sulfur-vacancy-rich ZIS/MoS_2/Mo heterostructure is constructed, in which a magnetic-field-induced micro-potential is harnessed to regulate charge dynamics and enable efficient H_2 evolution. Under a rotating magnetic field, metallic Mo component generates a motional electromotive force, thereby establishing a wireless internal electric field that spatially directs the migration of photogenerated electrons and holes in opposite directions. Owing to the synergistic interplay among sulfur vacancies, heterointerface engineering, and the magnetically induced micro-potential, the optimized ZIS_v/MoS_{2-x}/Mo catalyst delivers a hydrogen evolution rate of 5.19 $mmol \cdot g^{-1} \cdot h^{-1}$, which is 10.4-fold higher than that of pristine ZIS and represents an approximately 50% enhancement relative to the non-magnetic-field condition. Meanwhile, an apparent quantum yield of 20.98% is achieved at 380 nm. Systematic experimental characterizations, together with COMSOL simulations and density functional theory (DFT) calculations, demonstrate that the induced micro-potential significantly accelerates charge carriers separation and directional transport, while sulfur vacancies act as active electron-trapping centers that further promote charge utilization efficiency. This work establishes a magnetically engineered wireless electric-field strategy for rationally manipulating charge dynamics and boosting photocatalytic performance.

KEYWORDS: ZIS_v/MoS_{2-x}/Mo, magnetic field, micro-potential, S vacancies, photocatalytic H_2 evolution

Just Accepted

1 Introduction

The escalating global energy crisis and environmental pollution have driven an urgent demand for clean and renewable energy alternatives. As an ideal zero-carbon energy carrier, hydrogen (H_2) has attracted extensive research attention. Photocatalytic hydrogen evolution (PHE) using semiconductor catalysts is widely regarded as a sustainable and environmentally friendly approach for solar-to-chemical energy conversion [1-6]. However, the practical application of photocatalytic H_2 evolution is severely hindered by low light-harvesting efficiency, rapid recombination of photogenerated electron-hole pairs, and poor utilization of charge carriers. Therefore, developing effective strategies to address these challenges is crucial for advancing high-performance photocatalysts.

Metal sulfides photocatalyst, including PbS, CdS, ZnS, and $ZnIn_2S_4$ (ZIS), have been extensively explored owing to their suitable band structures and strong visible-light absorption [7-11]. Among them, ZIS features a tunable band gap of 2.1-2.9 eV and has emerged as a promising candidate for photocatalysis [12,13]. Nevertheless, the rapid charge recombination in pristine ZIS significantly restricts its photocatalytic activity. To overcome this limitation, defect engineering and heterostructure construction have been widely established as two effective strategies [14-20]. The introduction of anion vacancies (e.g., S vacancies, O vacancies) as effective electron “traps” in photocatalysts plays an important role in not only accelerating the separation of photo-induced charge carriers but also enhancing light absorption capability [21,22]. However, defect introduction alone is insufficient to achieve effective photocatalytic activity. Constructing heterostructures via band structure matching is another efficient strategy for enhancing photocatalytic efficiency [23-26]. The formation of heterostructures generates a built-in electric field that drives directional charge transfer and suppresses charge recombination [27-29].

Beyond the built-in electric field induced by heterostructures, external fields such as magnetic fields (MF) offer a non-contact and convenient strategy to further enhance charge separation [30-32]. According to the principle of electromagnetic

Just Accepted

induction, when metallic conductors move perpendicularly through a magnetic field, a motional electromotive force is generated. The Lorentz force subsequently redistributes electrons and holes, forming a local micro-potential that promotes charge separation. Ultimately, the photocatalytic performance of metal-based nanomaterials is enhanced under a MF [33]. Despite these advantages, the synergistic integration of heterostructure design, vacancy engineering, and magnetic-field-induced micro-potential for enhancing photocatalytic performance has rarely been reported.

In this work, a sulfur-vacancy-rich ZIS_v/MoS_{2-x}/Mo heterostructure was successfully synthesized via a two-step hydrothermal method. A distinct micro-potential is generated by metallic Mo sheets under a rotating MF, which, in synergy with S vacancies and the heterostructure, significantly promotes charge separation and photocatalytic activity. Under magnetic-field conditions, the PHE performance is markedly enhanced. The generation and distribution of the micro-potential are verified by COMSOL simulations, while the electronic structure and charge-transfer mechanism are elucidated by DFT calculations. A new paradigm for enhancing photocatalytic activity is thereby provided through the integration of magnetic-field engineering, defect engineering, and heterostructure construction.

2 Experimental

2.1 Synthesis of the ZIS/MoS_2/Mo heterostructure

Metallic Mo sheets (192 mg, 2 mmol) were uniformly dispersed in a mixed solution of deionized water (40 mL) and ethanol (20 mL) via ultrasonication and stirring for 30 min, respectively. Afterwards, $InCl_3 \cdot 4H_2O$ (1173 mg, 4 mmol), $Zn(CH_3COO)_2 \cdot 2H_2O$ (439 mg, 2 mmol), and thioacetamide (1203 mg, 16 mmol) were successively added and dissolved in the suspension. The mixture was transferred into a Teflon-lined stainless steel autoclave and heated at 200 °C for 24 h. The gray product was collected by centrifugation, thoroughly washed with deionized water and ethanol, and dried under vacuum at 70 °C overnight.

Just Accepted

2.2 Synthesis of S-vacancy-rich ZIS_v/MoS_{2-x}/Mo heterostructure

As-prepared ZIS/MoS_2/Mo powder (300 mg) was dispersed in 60 mL deionized water with continuous ultrasonication and magnetic stirring for 30 min. Hydrazine hydrate ($N_2H_4 \cdot H_2O$, 15 mL) was then added dropwise, and the mixture was stirred for 1 h to introduce sulfur vacancies. The resulting suspension was transferred into a Teflon-lined autoclave and heated at 240 °C for 5 h. The final product was collected by centrifugation at 10000 rpm for 6 min, washed thoroughly with deionized water, and dried under vacuum at 70 °C overnight.

2.3 Photoelectrochemical measurements

All photoelectrochemical tests were carried out on a CHI660E electrochemical workstation equipped with a standard three-electrode system. A platinum sheet served as the counter electrode, and an Hg/HgO electrode was used as the reference electrode. The working electrode was fabricated by coating catalyst slurry onto fluorine-doped tin oxide (FTO) glass. A 300 W xenon lamp was used as the light source, and 0.5 M Na_2SO_4 aqueous solution (pH = 7) acted as the supporting electrolyte. Electrochemical impedance spectroscopy (EIS) was measured at the open-circuit potential. Transient photocurrent (I-t) curves were recorded at a bias voltage of 0.1 V under periodic light irradiation and magnetic field switching.

2.4 PHE measurements

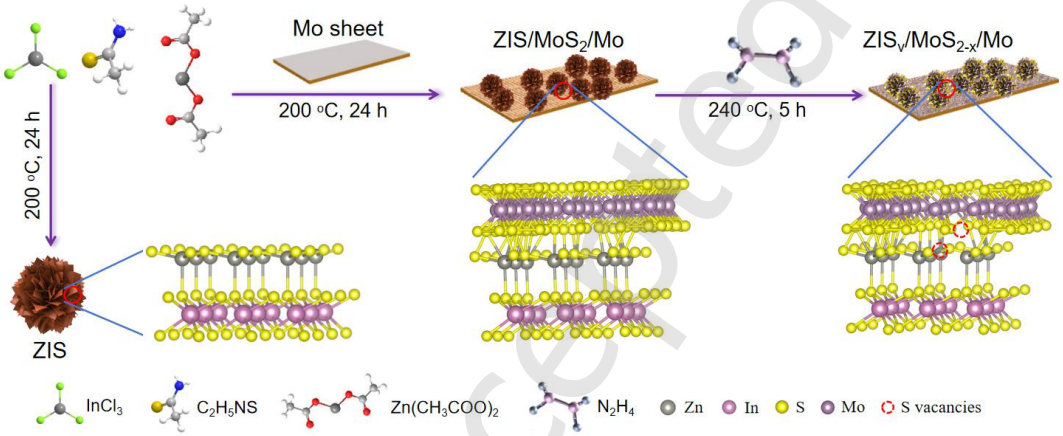
The PHE performance was evaluated on a dedicated photocatalytic analysis system. Typically, 20 mg of photocatalyst was uniformly dispersed in 50 mL of mixed aqueous solution containing 0.25 M Na_2SO_3 and 0.35 M Na_2S via ultrasonication and stirring. A 300 W xenon lamp with a 420 nm cut-off filter was vertically placed above the reactor to provide simulated sunlight due to the visible light characteristics of the photocatalysts. Thus, the photocatalytic performance test was conducted under visible light conditions. The light intensity was calibrated using an optical power meter. Circulating cooling water at 10 °C was applied to maintain a stable reaction

Just Accepted

temperature. The generated H_2 gas was quantitatively analyzed using a GC7920-TF2A gas chromatograph equipped with a thermal conductivity detector (Beijing China Education Au-light Co., Ltd.).

3 Results and discussion

3.1 Preparation and characterization of the ZIS_v/MoS_{2-x}/Mo heterostructure



Scheme 1 Schematic illustration of the synthesis of ZIS/MoS_2/Mo and ZIS_v/MoS_{2-x}/Mo heterostructures.

The ZIS/MoS_2/Mo heterostructure was prepared by a one-step hydrothermal method, and S vacancies were further introduced via hydrazine hydrate ($N_2H_4 \cdot H_2O$) reduction (Scheme 1). The morphological characteristics of the synthesized samples were investigated by SEM, TEM, and HR-TEM. As shown in Fig. S1(a) in the ESM, metallic Mo sheets exhibit lateral sizes ranging from 0.5 to 7 μm with smooth surfaces. The TEM image further confirms the sheet-like morphology of the Mo sample (Fig. S1(d) in the ESM). SEM and TEM analyses reveal that ZIS nanoflowers are uniformly grown on the surface of metallic Mo sheets (Figs. 1(a) and 1(b)). The HR-TEM image displays distinct lattice fringes with spacings of 0.32 and 0.63 nm, corresponding to the (102) plane of ZIS and the (002) plane of MoS_2, respectively (Fig. 1(c)) [34,35]. The introduction of S vacancies in the photocatalysts exerts no obvious influence on the morphological structure (Figs. S1 and S2 in the ESM). The crystal structure of the photocatalysts was characterized by XRD. The three main

Just Accepted

diffraction peaks at 40.5°, 58.6°, and 73.7° observed for the prepared metallic Mo sheets are assigned to metallic Mo (JCPDS No. 42-1120). The additional weak peaks can be indexed to MoO_2 (JCPDS No. 78-1069), originating from slight oxidation of Mo upon exposure to air (Fig. S3 in the ESM), which is beneficial for the subsequent formation of MoS_2 during the sulfidation process. The diffraction peaks of the ZIS/MoS_2/Mo heterostructure are attributed to hexagonal-phase $ZnIn_2S_4$ (JCPDS No. 65-2023) and metallic Mo (Fig. 1(d)). The diffraction peaks of MoS_2 were not detected due to its poor crystallinity [36-38]. The introduction of S vacancies in the photocatalysts does not exert an obvious influence on the crystal structure. In addition, the Raman spectra were employed to investigate the chemical structure of the samples (Fig. S4 in the ESM). The characteristic peak at 400 cm^{-1} could be assigned to the MoS_{2-x} [39]. The corresponding peak could also be observed in the ZIS_v/MoS_{2-x}/Mo heterostructure, indicating the successful synthesis of this photocatalyst. Electron paramagnetic resonance (EPR) spectroscopy was employed to elucidate the presence of S vacancies in the photocatalysts (Fig. 1(e)). No EPR signal is observed for pristine ZIS. In contrast, ZIS_v exhibits a pronounced signal at a g-factor of 2.008 compared with pristine ZIS. In addition, the EPR intensity of the ZIS_v/MoS_{2-x}/Mo heterostructure is increased by 25.8% relative to ZIS_v, owing to the formation of S vacancies in both ZIS and MoS_2, which increases the number of unpaired electrons. These EPR results demonstrate the abundant S vacancies in the ZIS_v/MoS_{2-x}/Mo heterostructure.

Just Accepted

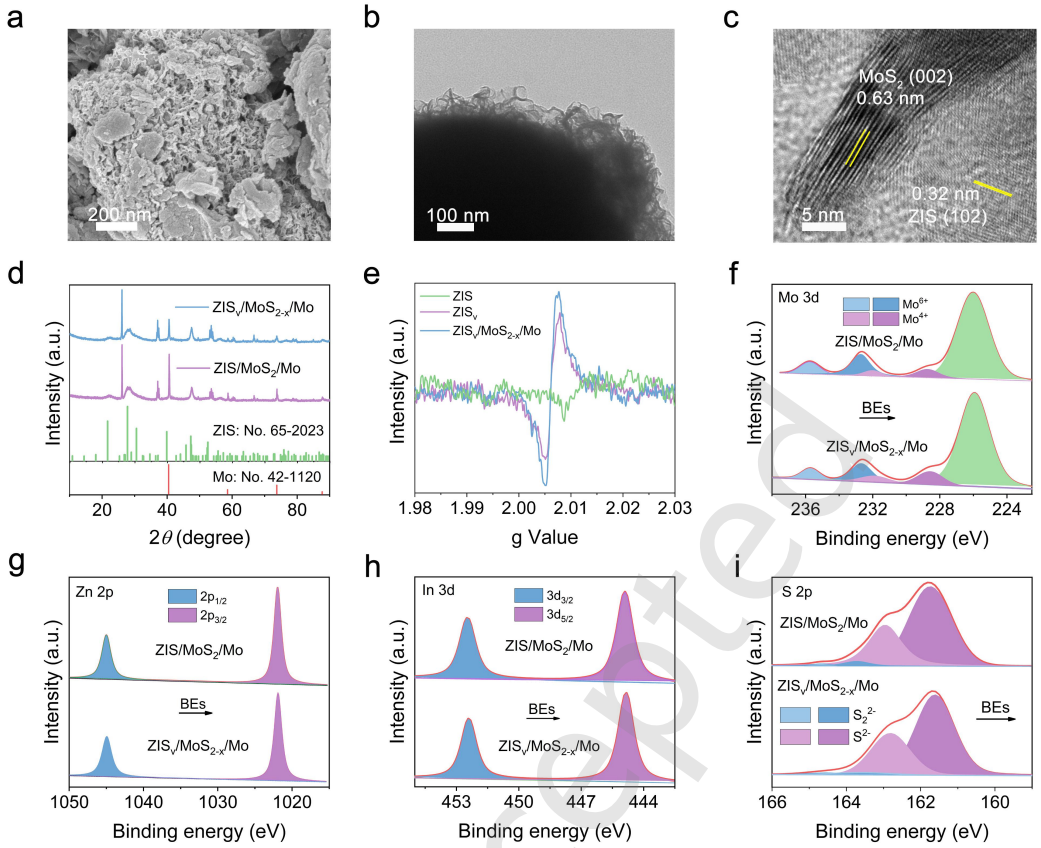


Figure 1 (a) SEM, (b) TEM, and (c) HR-TEM images of the ZIS_v/MoS_{2-x}/Mo heterostructure. (d) XRD patterns of the ZIS/MoS_2/Mo and ZIS_v/MoS_{2-x}/Mo heterostructure. (e) EPR spectra of ZIS, ZIS_v and the ZIS_v/MoS_{2-x}/Mo heterostructure. High- resolution XPS spectra for (f) Mo 3d, (g) Zn 2p, (h) In 3d, and (i) S 2p of the ZIS/MoS_2/Mo and ZIS_v/MoS_{2-x}/Mo heterostructure.

The chemical composition and surface chemical states of the samples were analyzed by XPS. In the Mo 3d XPS spectrum of the ZIS/MoS_2/Mo heterostructure, the peaks at 235.73 and 232.70 eV are assigned to the Mo^{6+} $3d_{3/2}$ and Mo^{6+} $3d_{5/2}$ doublets, respectively (Fig. 1(f)). The peaks at 232 and 228.71 eV are assigned to Mo^{4+} $3d_{3/2}$ and Mo^{4+} $3d_{5/2}$, respectively. Upon the formation of S vacancies, the corresponding peaks of the ZIS_v/MoS_{2-x}/Mo heterostructure for Mo^{4+} $3d_{3/2}$, Mo^{4+} $3d_{5/2}$, Mo^{6+} $3d_{3/2}$, and Mo^{6+} $3d_{5/2}$ are shifted to 231.90, 228.57, 235.71, and 232.68 eV, respectively. In addition, the Zn 2p XPS spectrum of the ZIS/MoS_2/Mo heterostructure shows doublet peaks at 1045 and 1021.95 eV, corresponding to Zn $2p_{1/2}$ and $2p_{3/2}$, respectively (Fig. 1(g)). In comparison, the corresponding peaks of the ZIS_v/MoS_{2-x}/Mo heterostructure are shifted toward lower binding energies (BEs) by 0.11 and 0.12 eV, respectively. Furthermore, the peaks located at 452.47 and 444.89

Just Accepted

eV are attributed to the In $3d_{3/2}$ and $3d_{5/2}$ doublets of the ZIS/MoS_2/Mo heterostructure, which are shifted toward lower binding energies of 452.38 and 444.80 eV in the ZIS_v/MoS_{2-x}/Mo sample, respectively (Fig. 1(h)). As for the ZIS/MoS_2/Mo heterostructure, the S $2p_{1/2}$ and $2p_{3/2}$ doublets are located at 164.67 and 163.71 eV, while S_2^{2-} $2p_{1/2}$ and S_2^{2-} $2p_{3/2}$ doublets are located at 162.95 and 161.73 eV, respectively (Fig. 1(i)). The deconvoluted peaks of the ZIS_v/MoS_{2-x}/Mo heterostructure at 164.54 and 163.59 eV are attributed to the S $2p_{1/2}$ and $2p_{3/2}$ doublets, while the peaks at 162.82 and 161.62 eV are assigned to S_2^{2-} $2p_{1/2}$ and S_2^{2-} $2p_{3/2}$, respectively. The presence of abundant S vacancies may account for the decreased binding energies observed in the ZIS_v/MoS_{2-x}/Mo heterostructure compared with the ZIS/MoS_2/Mo heterostructure. The S vacancies play an important role in strong electron-withdrawing group to facilitate the electrons of ZIS and MoS_2 transfer to S vacancies. Therefore, the equilibrium electron cloud density of S atoms inside ZIS and MoS_2 is decreased, resulting in the decrease of binding energy. In addition, the detailed XPS results of ZIS, ZIS_v, the ZIS/MoS_2 and ZIS_v/MoS_{2-x} exhibit similar trends to those of the ZIS_v/MoS_{2-x}/Mo heterostructure, further confirming the influence of S vacancies (Figs. S5 and S6 in the ESM).

3.2 Photocatalytic performance analysis for H_2 evolution

The PHE reaction under a magnetic field (MF) and non-magnetic field (NMF) was employed to evaluate the role of MF in the catalytic performance of the samples. The Fig. 2(a) illustrated the PHE reaction equipment with a rotating MF generator. Two permanent magnets were used to produce MF with the surface intensity of 950 Gauss (Fig. S7 in the ESM). The MoS_2/Mo sample produced no detectable hydrogen after 4 h of reaction under both MF and NMF conditions (Fig. 2(b)). The other photocatalysts showed stable PHE rate under 4 hours reaction under NMF or MF conditions (Fig. S8 in the ESM). The pristine ZIS exhibits low PHE rates of 0.52 and 0.64 $mmol \cdot g^{-1} \cdot h^{-1}$ under NMF and MF conditions, respectively. The 22% enhancement in the PHE rate of ZIS under the MF condition can be attributed to the Lorentz force, which suppresses electron-hole recombination and drives their migration in opposite

Just Accepted

directions. In comparison, ZIS_v shows enhanced PHE rates of 0.75 and 0.91 $mmol \cdot g^{-1} \cdot h^{-1}$ under NMF and MF conditions, which are 1.44 and 1.42 times higher than those of pristine ZIS, respectively. The improved PHE performance of ZIS_v is attributed to the presence of S vacancies, which serve as electron traps to promote the separation of photogenerated charge carriers. In addition, the ZIS/MoS_2 heterostructure exhibits a PHE rate of 1.24 $mmol \cdot g^{-1} \cdot h^{-1}$ under NMF conditions, which is 2.38 times higher than that of pristine ZIS. The construction of the ZIS/MoS_2 heterostructure and the introduction of MoS_2 active sites exert a significant effect on enhancing the PHE activity. Under MF conditions, the PHE rate of ZIS/MoS_2 reaches 1.53 $mmol \cdot g^{-1} \cdot h^{-1}$, and the 23% improvement is attributed to the Lorentz force induced by the magnetic field. In comparison, the ZIS_v/MoS_{2-x} heterostructure exhibits enhanced PHE rates of 2.15 and 2.58 $mmol \cdot g^{-1} \cdot h^{-1}$ under NMF and MF conditions, respectively, which are 1.58 and 1.69 times higher than those of ZIS/MoS_2, owing to the synergistic effects of S vacancies and the MF. As for the ZIS/MoS_2/Mo heterostructure, the PHE rates are 2.44 and 3.77 $mmol \cdot g^{-1} \cdot h^{-1}$ under NMF and MF conditions, respectively. The PHE rate under MF conditions is significantly enhanced by 55% compared with that of ZIS/MoS_2/Mo under NMF conditions, which is attributed to the micro-potential generated by metallic Mo sheets in the ZIS/MoS_2/Mo heterostructure according to the theory of electromagnetic induction. The PHE rate of ZIS/MoS_2/Mo heterostructure is enhanced 97% compared to the ZIS/MoS_2 heterostructure under NMF conditions due to the Mo substrate plays a significant role in the bridge of charge transfer, leading to the enhancement of photocatalytic performance. In addition, the ZIS_v/MoS_{2-x}/Mo heterostructure exhibits a PHE rate of 3.52 $mmol \cdot g^{-1} \cdot h^{-1}$ under NMF conditions, representing a 44% enhancement compared with ZIS/MoS_2/Mo, owing to the contribution of S vacancies. Notably, the ZIS_v/MoS_{2-x}/Mo heterostructure delivers the highest PHE rate of 5.19 $mmol \cdot g^{-1} \cdot h^{-1}$ under MF conditions among all photocatalysts, which is 1.47 times higher than that under NMF conditions, attributable to the positive influence of the micro-potential. Moreover, the PHE rate of ZIS_v/MoS_{2-x}/Mo under MF conditions is 10.4 times higher than that of ZIS under NMF conditions, arising from the synergistic effect of

Just Accepted

heterostructure construction, S vacancies, and the magnetic-field-induced micro-potential.

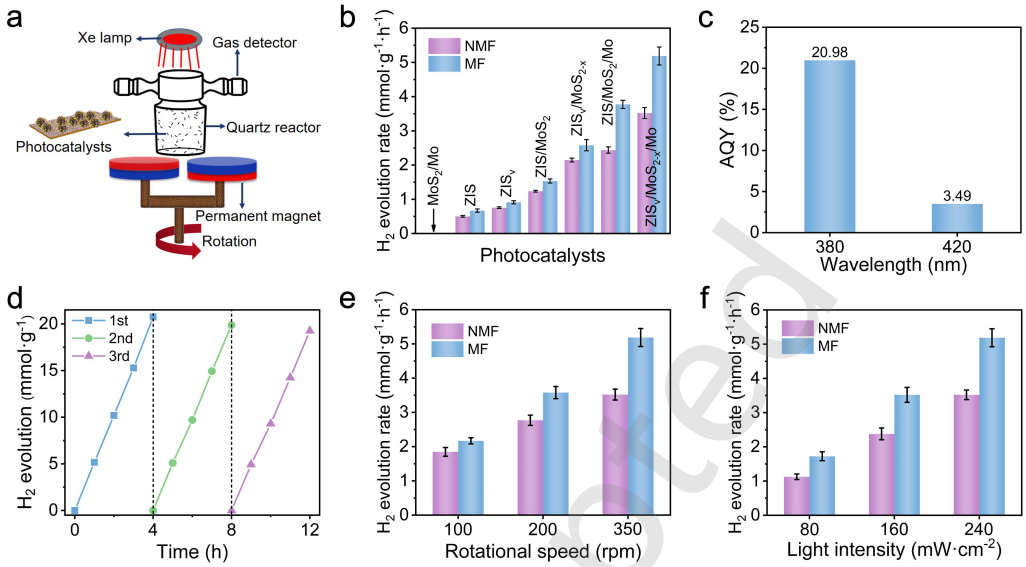


Figure 2 (a) Schematic diagram of the PHE reaction device under the influence of MF. (b) PHE rates of the photocatalysts under NMF and MF conditions. (c) Wavelength-dependent AQY of the $ZIS_v/MoS_{2-x}/Mo$ heterostructure. (d) Cyclic stability of the $ZIS_v/MoS_{2-x}/Mo$ heterostructure for PHE reaction. (e) PHE rates of the $ZIS_v/MoS_{2-x}/Mo$ heterostructure with different rotation rate under NMF and MF conditions. (f) PHE rates of the $ZIS_v/MoS_{2-x}/Mo$ heterostructure with different light intensities under NMF and MF conditions.

In addition, the wavelength-dependent apparent quantum yield (AQY) of the $ZIS_v/MoS_{2-x}/Mo$ heterostructure was calculated and shown in Fig. 2(c). The measurements were performed using a procedure similar to that of the PHE reaction, except that a band-pass filter was employed to provide monochromatic irradiation (λ=380 and 420 nm). The detailed measurements, the power of monochromatic irradiation, and the corresponding calculation results are presented in Table S1 in the ESM. The AQY values of the $ZIS_v/MoS_{2-x}/Mo$ heterostructure are calculated to be 20.98% and 3.49% at wavelengths of 380 and 420 nm, respectively, indicating its excellent light absorption and charge carriers utilization capability. The cycling stability test shows that the $ZIS_v/MoS_{2-x}/Mo$ heterostructure retains 93% of its PHE activity after three reaction cycles, demonstrating its favorable photocatalytic stability

Just Accepted

and durability (Fig. 2(d)). Furthermore, the effects of rotational speed and light intensity on the PHE performance of the ZIS_v/MoS_{2-x}/Mo heterostructure were evaluated. The heterostructure exhibits relatively low PHE rates of 1.13 and 1.72 $mmol \cdot g^{-1} \cdot h^{-1}$ at a rotational speed of 100 rpm under NMF and MF conditions, respectively (Fig. 2(e)). When the rotational speed is increased to 200 rpm, the PHE rates rise to 2.38 and 3.52 $mmol \cdot g^{-1} \cdot h^{-1}$ under NMF and MF conditions, respectively. In comparison, this heterostructure exhibits the highest PHE rates of 3.52 and 5.19 $mmol \cdot g^{-1} \cdot h^{-1}$ at a rotational speed of 350 rpm under NMF and MF conditions, respectively. The PHE rates of the ZIS_v/MoS_{2-x}/Mo heterostructure are enhanced by 0.32, 0.81, and 1.67 $mmol \cdot g^{-1} \cdot h^{-1}$ at rotational speeds of 100, 200, and 350 rpm, respectively, under the influence of the magnetic field. As described by the motional electromotive force formula:

$$\varepsilon = BLV$$

The potential is proportional to the relative motion speed. Accordingly, increasing the rotational speed elevates the micro-potential and further facilitates charge separation, thereby enhancing H_2 evolution. In addition, the PHE rates of the ZIS_v/MoS_{2-x}/Mo heterostructure increase with gradually increasing light intensity (Fig. 2(f)). The PHE rates of the ZIS_v/MoS_{2-x}/Mo heterostructure are 0.60, 1.14, and 1.67 $mmol \cdot g^{-1} \cdot h^{-1}$ at low, medium, and high light intensities (80, 160, and 240 $mW \cdot cm^{-2}$) under MF conditions, respectively. It is inferred that more photogenerated charge carriers are generated under higher light intensity, and their separation is further promoted by the magnetic-field-induced micro-potential, enabling enhanced PHE performance.

3.3 Photoelectrochemical and optical performance measurements

The photocurrent responses and electrochemical impedance spectroscopy (EIS) measurements were conducted to investigate the photoelectrochemical properties of the photocatalysts. The photoelectrochemical setup consisted of a three-electrode system coupled with a MF generator, which was positioned facing the right side of the working electrode at a constant rotational speed (Fig. 3(d)). The photocurrent

Just Accepted

response results were displayed in Fig. 3(a). The photocurrent of ZIS_v is higher than that of ZIS under light irradiation due to the formation of S vacancies (Fig. S9(a) in the ESM), indicating enhanced photoinduced charge generation in the photocatalysts. In addition, the introduction of a MF further increases the photocurrent of both ZIS and ZIS_v, which is attributed to the Lorentz force (Fig. S10 in the ESM). The photocurrent densities of the ZIS/MoS_2 and ZIS_v/MoS_{2-x} heterostructures are 1.2 and 2.6 $\mu A \cdot cm^{-2}$ under NMF conditions, respectively, indicating that the introduction of S vacancies facilitates electron migration. The photocurrent responses of both ZIS_v/MoS_{2-x} and ZIS/MoS_2 heterostructures are further enhanced under MF conditions compared with those under NMF conditions. Moreover, the average photocurrent densities of the ZIS/MoS_2/Mo and ZIS_v/MoS_{2-x}/Mo heterostructures are 7.4 and 14.9 $\mu A \cdot cm^{-2}$ under NMF conditions, respectively, attributable to the contribution of S vacancies. The ZIS_v/MoS_{2-x}/Mo heterostructure exhibits the highest photocurrent intensity among all photocatalysts under MF conditions, indicating that the micro-potential generated by metallic Mo sheets efficiently promotes electron migration. The ZIS_v/MoS_{2-x}/Mo heterostructure shows the best photocurrent performance among all photocatalysts over two cycles under alternating light irradiation and MF at 50 s intervals. To further elucidate the role of the rotating MF in the ZIS_v/MoS_{2-x}/Mo heterostructure, the effects of rotation rate and MF intensity on the dark current density were systematically investigated. As displayed in Fig. 3(b), the average current density of the ZIS_v/MoS_{2-x}/Mo heterostructure in the dark at different rotation rates (100, 200, and 350 rpm) is measured to be 1.0, 2.2, and 3.7 $\mu A \cdot cm^{-2}$ under MF conditions, respectively. The pronounced increase in current with increasing rotation rate is attributed to the fact that the current magnitude is approximately proportional to the rate of magnetic flux cutting.

Just Accepted

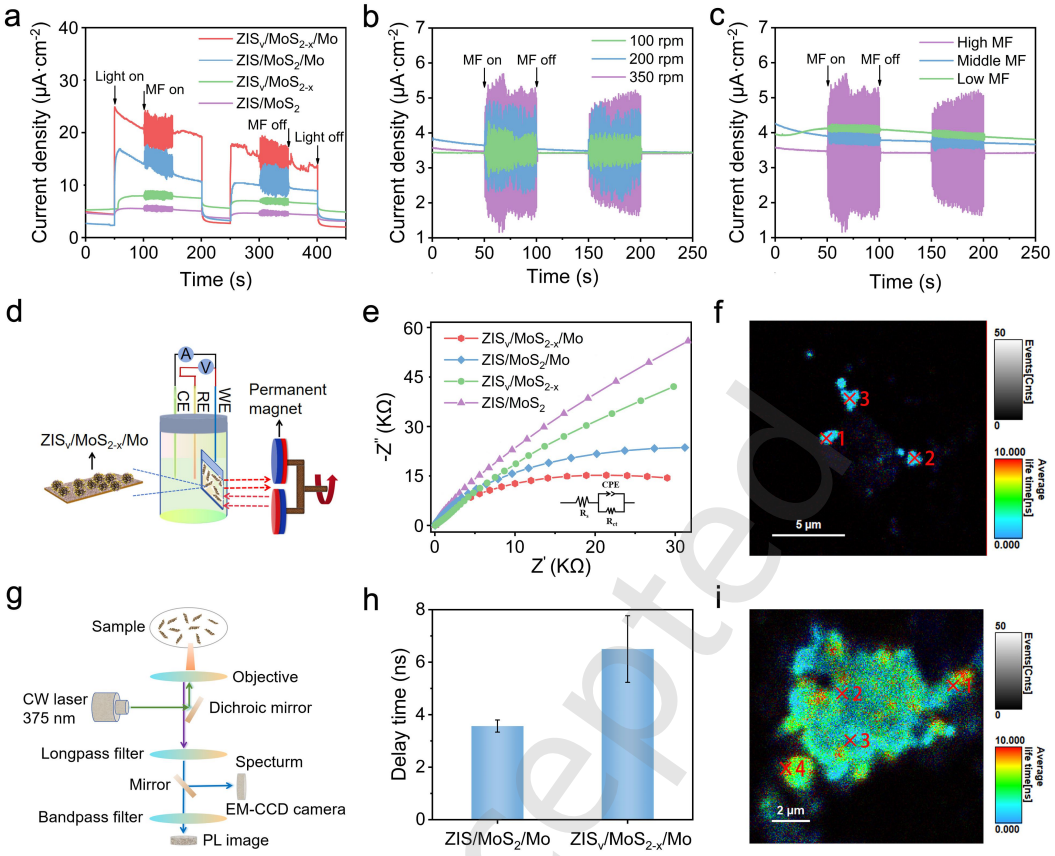


Figure 3 (a) Photocurrent responses of the photocatalysts under light and MF conditions. (b) Current density of the ZIS$_v$/MoS$_{2-x}$/Mo heterostructure with different rotation rate in the dark. (c) Current density of the ZIS$_v$/MoS$_{2-x}$/Mo heterostructure in the dark with different magnetic field intensity by controlling the distant of two magnets to FTO for 1, 6, and 11 cm, respectively. (d) Schematic of the photoelectrochemical testing device under MF. (e) EIS curves of the photocatalysts. (f) Single particle PL mapping images of the ZIS/MoS$_2$/Mo heterostructure. (g) Schematic of single-particle PL measurement. (h) Single particle time-resolved PL spectra. (i) Single particle PL mapping images of the ZIS$_v$/MoS$_{2-x}$/Mo heterostructure.

In addition, low-, medium-, and high-intensity magnetic fields were established by adjusting the distance between two magnets and the FTO electrode to 1, 6, and 11 cm, respectively. The average dark current density of the ZIS$_v$/MoS$_{2-x}$/Mo heterostructure under low, medium, and high MF conditions is calculated to be 0.2, 0.4, and 3.7 μA·cm^{-2}, respectively (Fig. 3(c)). This result indicates that a high magnetic field is favorable for generating a larger current in the ZIS$_v$/MoS$_{2-x}$/Mo heterostructure, consistent with the theory of electromagnetic induction. The current

Just Accepted

response remains relatively stable over two cycles under alternating MF on/off intervals of 50 s. In addition, the EIS spectra reveal that the charge-transfer resistance (R_{ct}) follows the order of ZIS > ZIS_v > ZIS/MoS_2 > ZIS_v/MoS_{2-x} > ZIS/MoS_2/Mo > ZIS_v/MoS_{2-x}/Mo, indicating progressively improved charge-transfer kinetics (Figs. 3(e) and S9(b)). The ZIS_v/MoS_{2-x}/Mo heterostructure exhibits the smallest semicircle radius among all photocatalysts, indicating that the construction of the heterostructure and the introduction of S vacancies effectively reduce interfacial charge-transfer resistance. Furthermore, a time-resolved single-particle photoluminescence (PL) lifetime imaging microscopy system was employed to obtain single-particle PL images and fluorescence lifetimes of the photocatalysts (Fig. 3(g)). The single-particle PL images are presented, and the average lifetime increases from blue to red in the color scale. The single-particle PL image of ZIS_v/MoS_{2-x} appears deeper in color than that of the ZIS/MoS_2 heterostructure (Figs. S11(a-c) in the ESM). The average lifetimes of the ZIS/MoS_2 and ZIS_v/MoS_{2-x} heterostructures are calculated to be 3.0 and 5.6 ns, respectively, indicating that the introduction of S vacancies can effectively extend the charge carriers lifetime in ZIS/MoS_2 (Fig. S11(d) in the ESM). In addition, the single-particle PL image of ZIS_v/MoS_{2-x}/Mo is significantly deeper in color than that of the ZIS/MoS_2/Mo heterostructure (Figs. 3(f) and 3(i)). The average lifetime of ZIS/MoS_2/Mo and ZIS_v/MoS_{2-x}/Mo heterostructure were 3.6 and 6.5 ns, respectively (Fig. 3(h)). The average lifetime of ZIS_v/MoS_{2-x}/Mo is prolonged by 80.6% compared with the ZIS/MoS_2/Mo heterostructure, owing to the contribution of S vacancies in efficiently suppressing charge recombination.

3.4 Band structure analysis

The band gap (E_g) values of the ZIS_v and MoS_{2-x} could be acquired from the Tauc plots [40].

$$(\alpha h\upsilon)^2 = A(h\upsilon - E_g)$$

where α, hν, and A represents the absorption coefficient, photon energy, and constant, respectively. The E_g values of the ZIS_v and MoS_{2-x} were determined to be 2.63 and 1.35 eV, respectively (Fig. 4(c)). Besides, the Mott-Schottky (M-S) plots

Just Accepted

were applied to analyze the flat band potential (E_{fb}) of the ZIS_v and MoS_{2-x}. As displayed in Figs. 4(a) and 4(b), the E_{fb} of the ZIS_v and MoS_{2-x} are determined to be -1.08 and -0.17 eV versus the normal hydrogen electrode (vs. NHE), respectively. The positive slope of the M-S plots for both ZIS_v and MoS_{2-x} confirms their n-type semiconductor characteristics. According to literature, the flat-band potential of an n-type semiconductor is approximately 0.2 eV more positive than its conduction band potential (E_{CB}) [28]. Thus, the E_{CB} of ZIS_v and MoS_{2-x} are determined to be -1.28 and -0.37 eV (vs. NHE), respectively. Accordingly, the valence band potentials (E_{VB}) of ZIS_v and MoS_{2-x} are calculated to be 1.35 and 0.98 eV (vs. NHE), respectively. The corresponding energy band structures of the ZIS_v/MoS_{2-x} heterostructure are therefore illustrated in Fig. 4(d). The introduction of double S vacancies in the ZIS_v/MoS_{2-x} heterostructure establishes new defect level, resulting in the increase of carriers concentration. The defect level enhances the transport of photogenerated electrons and prompts the separation efficiency of carriers in the ZIS_v/MoS_{2-x} heterostructure. Upon light irradiation, the photogenerated electrons are excited from the VB of ZIS_v to the defect level and subsequently transferred to its CB, leaving holes in the VB. When ZIS_v and MoS_{2-x} form the heterostructure, the photogenerated electrons are transferred from the CB or defect states of ZIS_v to the CB of MoS_{2-x}. Thus, S vacancies act as electron traps, enhancing the capture and separation of electrons. The electrons accumulated on the surface of MoS_{2-x} are then utilized for proton reduction to generate H_2, while the photogenerated holes at the VB of ZIS_v are partially consumed by the sacrificial agents. Other holes are transferred to the VB of MoS_{2-x} and then consumed by the sacrificial agents. However, efficient charge carriers transport from ZIS_v to the surface of MoS_{2-x} cannot be sufficiently achieved solely through the built-in electric field of the ZIS_v/MoS_{2-x} heterostructure.

Just Accepted

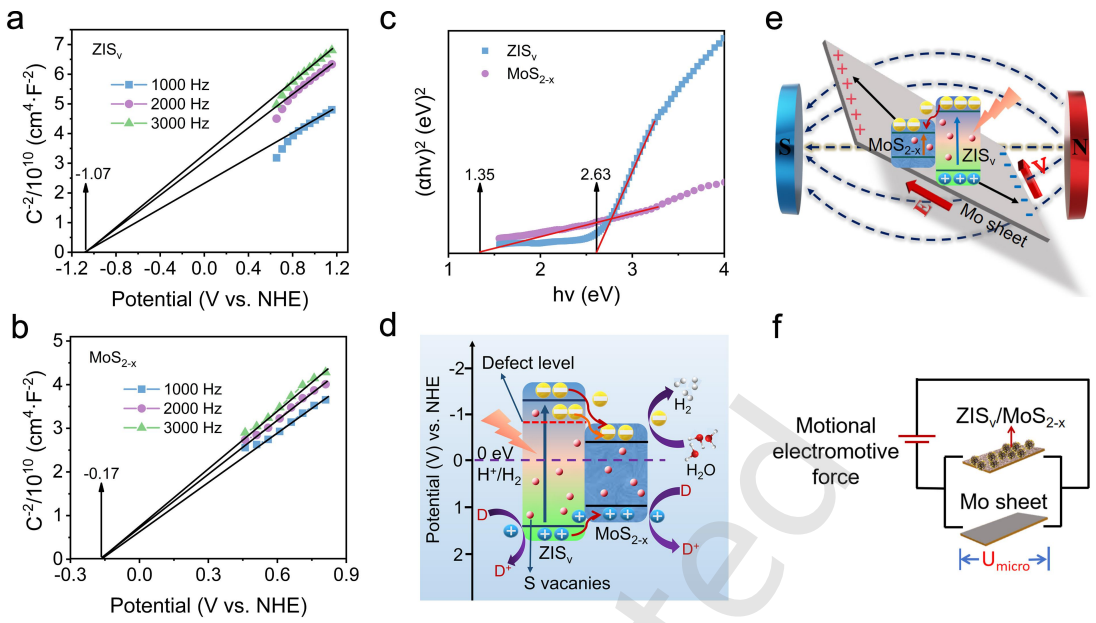


Figure 4 Mott-Schottky curves of (a) pure ZIS_v and (b) pure MoS_{2-x}. (c) Tauc plots of pure ZIS_v and pure MoS_{2-x}. (d) Schematic diagram of band alignment of the ZIS_v/MoS_{2-x} heterostructure. (e) Schematic diagram of the induced micro-potential to drive electrons and holes separation. (f) Schematic diagram of the motional electromotive force produced by the ZIS_v/MoS_{2-x} heterostructure and metallic Mo sheet.

Just Accepted

According to the theory of electromagnetic induction, a motional electromotive force is generated at both ends of a conductor when it moves in a magnetic field, thereby inducing charge migration. Furthermore, considering the sheet-like morphology of metallic Mo and the ZIS_v/MoS_{2-x}/Mo structure, the schematic diagrams illustrate a micro-potential both parallel and perpendicular to metallic Mo sheets, as well as an induced electric field that accelerates the separation of photogenerated charge carriers. The micro-potential is generated when both the position and motion direction of metallic Mo sheets are perpendicular to the magnetic field (Fig. S12 in the ESM). The micro-potential can accelerate the migration of electrons and holes in opposite directions on the photocatalyst surface and effectively suppress charge carriers recombination (Fig. 4(e)). On the other hand, when metallic Mo sheet is parallel to the magnetic field and its motion direction is perpendicular to the magnetic field, a micro-potential is generated at both ends of metallic Mo sheet, directed from the bottom to the top of the sheet (Fig. S13 in the ESM). A motional electromotive force is generated through the formation of the ZIS_v/MoS_{2-x}

heterostructure and the induced micro-potential of metallic Mo sheets (Fig. 4(f)). Thus, electrons and holes migrate in opposite directions on the photocatalyst surface under the effect of the motional electromotive force, enabling efficient charge carriers separation for H_2 evolution.

3.5 COMSOL multiphysics simulation

The micro-potential of metallic Mo sheets under a MF is evaluated using COMSOL Multiphysics simulations (Fig. 5). Based on the morphology and thickness of metallic Mo sheets, configurations with the sheets tilted, parallel, and perpendicular to the MF are constructed. A micro-potential is generated in metallic Mo sheet when its motion direction is oriented into the plane of the paper. According to the motional electromotive force equation, COMSOL simulation results show that the micro-potential of thin and thick metallic Mo sheets parallel to the MF is calculated to be 7.6×10^{-6} and 1.3×10^{-5} mV, respectively (Fig. 5(a)), indicating that the micro-potential increases with the thickness of metallic Mo sheets. The micro-potential distribution is consistent with the motional electromotive force according to the right-hand rule. When the tilt angle between metallic Mo sheet and the MF direction is approximately 45°, the micro-potential of thin and thick metallic Mo sheets is calculated to be 4.4×10^{-4} and 4.6×10^{-4} mV (Fig. 5(b)), respectively. In addition, the micro-potential of thin and thick metallic Mo sheets perpendicular to the MF is calculated to be 8.5×10^{-4} and 8.8×10^{-4} mV (Fig. 5(c)), respectively, which is approximately 1.9 times higher than that of the tilted configuration. Thus, the micro-potential intensity increases progressively from parallel to tilted to the perpendicular orientation relative to the MF. These results demonstrate that metallic Mo sheets in different orientations within the MF can all generate a micro-potential.

Just Accepted

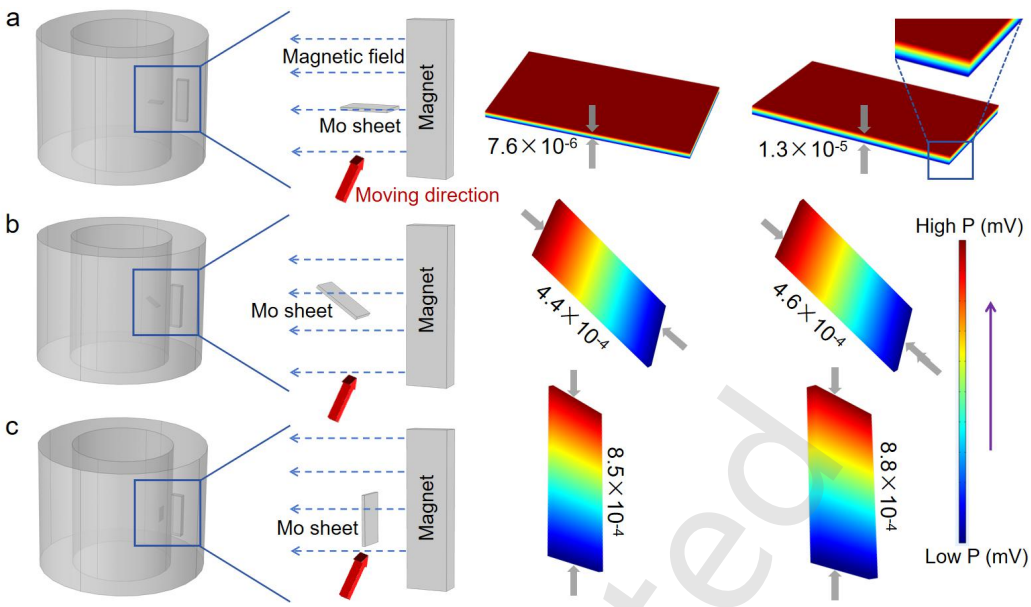


Figure 5 (a-c) COMSOL simulation of the micro-potential induced by metallic Mo sheets parallel, tilted, and perpendicular to MF, respectively.

3.6 DFT calculations

The DFT calculations are applied to further explore the PHE reaction mechanism of the photocatalysts. As shown in Fig. S14(a) in the ESM, when a single H atom is adsorbed on the upper surface of ZIS, the H adsorption energy of ZIS is calculated to be -1.21 eV (Fig. 6(a)). When a single H atom is adsorbed on the upper surface of MoS_2 in the ZIS/MoS_2 heterostructure (Fig. S14(b) in the ESM), the H adsorption energy reaches -2.30 eV, which is 1.90 times that of ZIS. This result indicates that the formation of the ZIS/MoS_2 heterostructure is beneficial for enhancing the adsorption ability of H atoms, thereby facilitating subsequent H_2 evolution. In addition, when a single H atom is adsorbed on the upper surface of MoS_{2-x} in the ZIS_v/MoS_{2-x} heterostructure (Fig. S14(c) in the ESM), the H adsorption energy is calculated to be -2.92 eV, which is 1.27 times that of the ZIS/MoS_2 heterostructure. The appropriate H adsorption energy enhancement demonstrates that the introduction of S vacancies in the ZIS_v/MoS_{2-x} heterostructure significantly improves the H atom adsorption capability. However, excessively strong H adsorption is detrimental to subsequent H desorption. Thus, the suitable increase in H adsorption energy is generally beneficial to the subsequent catalytic reactions. In addition, the charge density difference is

Just Accepted

calculated to analyze the electron migration. For the ZIS/MoS_2 heterostructure, electron depletion and accumulation mainly occur at the interface of ZIS and MoS_2, respectively (Fig. 6(b)). Besides, the variation of charge density is calculated by the Bader charge. There is 0.61 | e | transferred from ZIS to MoS_2 (Table S2 in the ESM), indicating the ZIS loses electrons and the MoS_2 obtains electrons, respectively. For the ZIS_v/MoS_{2-x} heterostructure, electrons accumulate at the lower surface of MoS_{2-x} and are depleted at the upper surface of ZIS_v, respectively (Fig. 6(c)). The Bader charge analysis shows that 1.52 | e | is transferred from ZIS_v to MoS_{2-x} in the ZIS_v/MoS_{2-x} heterostructure (Table S3 in the ESM), which is 2.49 times higher than that in the ZIS/MoS_2 heterostructure, indicating that the introduction of S vacancies promotes electron migration from ZIS_v to MoS_{2-x}.

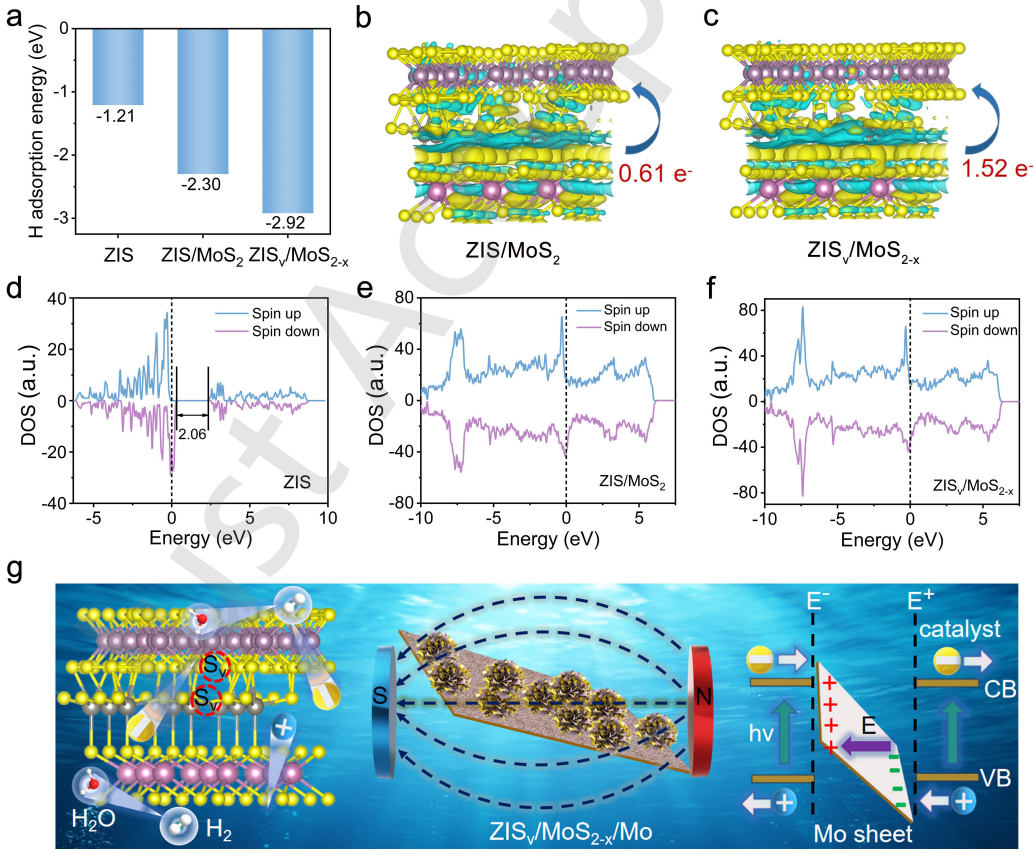


Figure 6 (a) The H adsorption energy of pure ZIS, the ZIS/MoS_2, and ZIS_v/MoS_{2-x} heterostructure. The side view of charge density difference and Bader charge of (b) the ZIS/MoS_2 and (c) ZIS_v/MoS_{2-x} heterostructure. TDOS spectra of (d) pure ZIS, (e) the ZIS/MoS_2, and (f) ZIS_v/MoS_{2-x} heterostructure. Dashed lines represent the Fermi level. (g) Schematic diagram of the PHE reaction on the surface of the ZIS_v/MoS_{2-x}/Mo heterostructure under the influence of MF to

Just Accepted

promote electrons and holes separation.

Furthermore, the projected density of states (PDOS) and total density of states (TDOS) of the photocatalysts are calculated to investigate their electrical conductivity. Pristine ZIS exhibits an obvious band gap of 2.06 eV near the Fermi level, confirming its semiconducting nature (Figs. 6(d) and S15). When ZIS and MoS_2 form a heterostructure, a continuous density of states appears near the Fermi level (Figs. 6(e) and S16). The DOS curve of the ZIS/MoS_2 heterostructure shows no obvious band gap, indicating enhanced electrical conductivity of the ZIS/MoS_2 heterostructure. In addition, the DOS intensity at the Fermi level for the ZIS_v/MoS_{2-x} heterostructure is higher than that of the ZIS/MoS_2 heterostructure (Figs. 6(f) and S17), indicating that the electrical conductivity is further improved by the introduction of S vacancies. The DFT calculation results demonstrate that both heterostructure construction and S vacancies introduction play significant roles in enhancing electron migration and H_2 evolution. As depicted in Fig. 6(g), the mechanism of the PHE reaction in the ZIS_v/MoS_{2-x}/Mo heterostructure involves the synergistic effect of S vacancies and the induced micro-potential. S vacancies in the ZIS_v/MoS_{2-x}/Mo heterostructure act as effective electron traps, thereby suppressing charge carriers recombination. Furthermore, the induced micro-potential facilitates improved charge carriers separation and migration. As a result, the PHE performance of the ZIS_v/MoS_{2-x}/Mo heterostructure is significantly enhanced.

4 Conclusions

In summary, a novel S-vacancy-rich ZIS_v/MoS_{2-x}/Mo heterostructure is prepared to achieve efficient PHE performance under MF conditions. The motional electromotive force is generated by the motion of metallic Mo sheets in a rotating magnetic field, according to the principle of electromagnetic induction. The magnetic-field-induced micro-potential provides a wireless electric field that significantly accelerates the separation and directional transport of photogenerated charge carriers. In addition, S

Just Accepted

vacancies in the ZIS_v/MoS_{2-x}/Mo heterostructure act as electron traps, promoting electron capture and utilization. The MoS_{2-x} component plays a crucial role in enabling rapid electron consumption for H_2 evolution. Owing to the synergistic effect of heterostructure construction, S vacancies, and micro-potential, the ZIS_v/MoS_{2-x}/Mo heterostructure achieves a high PHE rate of 5.19 $mmol \cdot g^{-1} \cdot h^{-1}$ under MF conditions, which is 10.4 times higher than that of pristine ZIS. The PHE rate of the ZIS_v/MoS_{2-x}/Mo heterostructure is enhanced by approximately 50% under MF conditions compared with that under NMF conditions, attributable to the contribution of the induced micro-potential. In addition, the ZIS_v/MoS_{2-x}/Mo heterostructure exhibits a high AQY of 20.98% at 380 nm, indicating excellent light absorption and charge carriers utilization capability. This study is expected to inspire further attention to the application of external magnetic fields in nanomaterial systems for achieving highly efficient photocatalytic activity.

Electronic Supplementary Material: Supplementary material (experimental procedures, detailed SEM and TEM images, XRD patterns, Raman spectra, XPS spectra, electrochemical test results, Single-particle PL mapping images, catalyst structural models and tables, photograph of samples) is available in the online version of this article at https://doi.org/10.26599/NR.2026.94909282.

Data availability

All data needed to support the conclusions in the paper are presented in the manuscript and the Electronic Supplementary Material. Additional data related to this paper may be requested from the corresponding author upon request.

Acknowledgements

The authors acknowledge the funding support from the National Natural Science Foundation of China (Grant Nos. 52102278, 22572104), the Natural Science Foundation of Shandong Province (Grant Nos. ZR2021ME207, ZR2025MS222, ZR2025QC2325Z, ZR2026QC2125Z), the Scientific Research Innovation Capability

Just Accepted

Support Project for Young Faculty (SRICSPYF-BS2025054), and the Qilu Young Scholars and Outstanding Young Scholars Projects of Shandong University.

Declaration of competing interest

All the contributing authors report no conflict of interests in this work.

Author contribution statement

C. C.: Data curation, project administration, validation, experimental design, writing manuscript. B. L.: Data curation, investigation, validation. L. W. Z.: Experimental design, investigation. W. C. Z.: Methodology. X. L. Z.: Formal analysis. X. N. W.: Project design. Y. H. S.: Project administration, project design. H. L.: Project administration, project design. Y. Z.: Project administration, project design, funding acquisition, revising manuscript. Z. K. Z.: Project administration, project design, funding acquisition, revising manuscript. All the authors have approved the final manuscript.

Use of AI statement

None.

References

[1] Yin, X. Y.; Gao, D. D.; Zhang, J. J.; García, H.; Yu, J. G.; Yu, H. G. Plasmon-induced ultrafast interfacial charge transfer for enhanced photocatalytic hydrogen evolution. *J. Am. Chem. Soc.* **2025**, *147*, 34881-34890.

[2] Chu, X. Y.; Liu, S. K.; Luan, B. B.; Zhang, Y.; Xi, Y. M.; Shao, L. H.; Zhang, F. M.; Lan, Y. Q. Crystal-facet-controlled internal electric field in MOF/COF heterojunction towards efficient photocatalytic overall water splitting. *Angew. Chem. Int. Ed.* **2025**, *64*, e202422940.

[3] Luan, B. B.; Chu, X. Y.; Wang, Y.; Qiao, X.; Jiang, Y. X.; Zhang, F. M. Construction of COF/COF organic S-Scheme heterostructure for enhanced overall water splitting. *Adv. Mater.* **2024**, *36*, 2412653.

[4] Nikoloudakis, E.; Lo´pez-Duarte, I.; Charalambidis, G.; Ladomenou, K.; Ince, M.; Coutsolelos, A. G. Porphyrins and phthalocyanines as biomimetic tools for photocatalytic H_2 production and CO_2 reduction. *Chem. Soc. Rev.* **2022**, *51*, 6965-7045.

[5] Qi, S. L.; Zhu, K. X.; Xu, T.; Zhang, H. F.; Guo, X. Y.; Wang, J. H.; Zhang, F. X.; Zong, X.

Just Accepted

Water-stable high-entropy metal-organic framework nanosheets for photocatalytic hydrogen production. *Adv. Mater.* **2024**, *36*, 2403328.

[6] Pan, Y. Y.; Zhang, B. X.; Ye, Z. W.; Shen, Y. F.; Hanish, J.; Wu, Y. P.; Malhotra, Y.; Li, K. J.; Norris, T. B.; Mi, Z. T. Excitonic quantum superlattices for efficient photocatalytic water splitting. *Nat. Energy* **2026**, *11*, 571-580.

[7] Tang, G. E.; Zhang, J. J.; Bie, C. B.; Zheng, X. S.; Jiang, C. J.; Yu, J. G. In situ soft X-ray absorption spectroscopy investigation on charge transfer mechanism in COF/CdS S-Scheme photocatalyst. *Adv. Mater.* **2025**, *37*, e14576.

[8] Han, Y. W.; Zhang, Y. X.; Ye, L.; Gong, T. J.; Lu, X. B.; Yan, N.; Fu, Y. Establishing dual-interface built-In electric fields within janus heterostructures for cooperative photoredox catalysis. *J. Am. Chem. Soc.* **2025**, *147*, 18637-18650.

[9] Liu, D. D.; Jiang, L. P.; Chen, D. Q.; Hao, Z. K.; Deng, B. W.; Sun, Y. Y.; Liu, X.; Jia, B. Y.; Chen, L. M.; Liu, H. T. Twin S-Scheme g-C_3N_4/$CuFe_2O_4$/$ZnIn_2S_4$ heterojunction with a self-Supporting three-phase system for photocatalytic CO_2 reduction: mechanism insight and DFT calculations. *ACS Catal.* **2024**, *14*, 5326-5343.

[10] Ruan, X. W.; Ding, C. S.; Jiao, D. X.; Leng, J.; Xu, M. H.; Li, B. N.; Yu, Z. P.; Cui, X. Q.; Yu, J. C.; Zhu, Y. F.; Ravi, S. K. Ga-on-In substitution with Zn vacancies in $Zn_3In_2S_6$ induces electron-hole asymmetry and In-O bond weakening for coupled two-electron oxygen reduction and H_2O_2 stabilization. *Adv. Mater.* **2026**, *38*, e22831.

[11] Ma, D.; Xu, M.; Ding, L.; Guo, J. K.; Yang, Y.; Dou,W.; Li, H.; Chen, F. J.; Tang, Y. Precise regulation of Zn, S dual vacancies in $Zn_3In_2S_6$ inducing local orientated electrical field for photocatalytic H_2O_2 generation. *Angew. Chem. Int. Ed.* **2025**, *65*, e21029.

[12] Song, Y. M.; Zheng, X. L.; Yang, Y. Q.; Liu, Y. H.; Li, J.; Wu, D. X.; Liu, W. F.; Shen, Y. J.; Tian, X. L. Heterojunction engineering of multinary metal sulfide-based photocatalysts for efficient photocatalytic hydrogen evolution. *Adv. Mater.* **2023**, *36*, 2305835.

[13] Gao, Z. X.; Liu, F. Y.; Chen, Z. W.; Song, Q.; Cullen, P. J.; Zhang, X. Y.; Zuo, Z. H.; Zhong, J.; Lu, X. Z.; Hu, Z. F.; Liu, R. Z.; Zhang, Q. Z.; Yin, Y. G.; Cai, Y. Defect-modulated oxygen adsorption and Z-scheme charge transfer for highly selective H_2O_2 photosynthesis in pure water. *Nat. Commun.* **2025**, *16*, 8889.

[14] Zhou, H.; Wang, H.; Yue, C. Y.; He, L. J.; Li, H.; Zhang, H.; Yang, S.; Ma, T. Y. Photocatalytic degradation by TiO_2-conjugated/coordination polymer heterojunction: Preparation, mechanisms, and prospects. *Appl. Catal. B Environ.* **2024**, *344*, 123605.

[15] Kment, Š.; Bakandritsos, A.; Tantis, I.; Kmentová, H.; Zuo, Y. P.; Henrotte, O.; Naldoni, A.; Otyepka, M.; Varma, R. S.; Zboril, R. Single atom catalysts based on earth-abundant metals for energy-related applications. *Chem. Rev.* **2024**, *124*,11767-11847.

[16] Muhammad, P.; Zada, A.; Rashid, J.; Hanif, S.; Gao, Y. A.; Li, C.; Li, Y. Y.; Fan, K.L.; Wang, Y. L. Defect engineering in nanocatalysts: from design and synthesis to applications. *Adv. Funct. Mater.* **2024**, *34*, 2314686.

Just Accepted

[17] Tan, Y.; Li, Y. M.;Wang, Y. H.; Zhao, X. Y.;Li, D. M.; Gong, S.; Li, Y. F.; Zhang, Y.; Wu Y. E. $Ir_xRu_{1-x}O_2/WO_3$ heterostructure for efficient acidic oxygen evolution reaction. *Nano Res.* **2026**, *19*, 94908622.

[18] Lazaar, N.; Wu, S. M.; Qin, S. S.; Hamrouni, A.; Sarma, B. B.; Doronkin, D. E.; Denisov, N.; Lachheb, H.; Schmuki, P. Single-atom catalysts on C_3N_4: minimizing single atom Pt loading for maximized photocatalytic hydrogen production efficiency. *Angew. Chem. Int. Ed.* **2025**, *64*, e202416453.

[19] Yuan, L.; Zhang, C. Q.; Zou, Y. Y.; Bao, T.; Wang, J.; Tang, C.; Du, A. J.; Yu, C. Z.; Liu, C. A S-Scheme MOF-on-MOF heterostructure. *Adv. Funct. Mater.* **2023**, *33*, 2214627.

[20] Zhang, X.; Zhou, Q. X.; Li, C.; Su, H.; Chen, T. R.; Cui, P. X.; Ban, C. G.; Tao, Y.; Wang, J. X.; Jiang, Y. H.; Liu, L. Y.; Teng, Z. Y.; Fan, Z. X.; Zhao, Y. X.; Zheng, K.; Ding, J.; Su, C. L.; Zhang, T. R.; Liu, B. Thermodynamic and kinetic modulation of artificial H_2O_2 photosynthesis via spatial control of redox catalytic sites. *J. Am. Chem. Soc.* **2026**, *148*, 11068-11080.

[21] Xu, M. H.; Ruan, X. W.; Meng, D. P.; Fang, G. Z.; Jiao, D. X.; Zhao, S. L.; Liu, Z. Y.; Jiang, Z. F.; Ba, K. K.; Xie, T. F.; Zhang, W.; Leng, J.; Jin, S. Y.; Ravi, S. K.; Cui, X. Q. Modulation of sulfur vacancies in $ZnIn_2S_4$/MXene schottky heterojunction photocatalyst promotes hydrogen evolution. *Adv. Funct. Mater.* **2024**, *34*, 2402330.

[22] Tang, Y.; Zhou, W.; Shang, Q. Q.; Guo, Y. C.; Hu, H. L.; Li, Z. Q.; Zhang, Y. Z.; Liu, L. Q.; Wang, H. Y.; Tan, X.; Yu, T.; Ye, J. H. Discerning the mechanism of expedited interfacial electron transformation boosting photocatalytic hydrogen evolution by metallic 1T-WS_2-induced photothermal effect. *Appl. Catal. B Environ.* **2022**, *310*, 121295.

[23] Shen, R. C.; Liang, G. J.; Hao, L.; Zhang, P.; Li, X. In situ synthesis of chemically bonded 2D/2D covalent organic frameworks/O-vacancy WO_3 Z-scheme heterostructure for photocatalytic overall water splitting. *Adv. Mater.* **2023**, *35*, 2303649.

[24] Xu, F. Y.; Zheng, L. X.; Zhang, J. J.; He, Y.; Cao, H.; Zheng, X. S.; García, H.; Yu, J. G. Co_3O_4 as full-solar-spectrum photocatalyst for selective methane conversion through reactive oxygen species control. *Nat. Catal.* **2026**, *9*, 73-86.

[25] Lv, K. X.; Li, Z. Z.; Huang, X.; Cheng, Z. T.; Wang, Z. Y.; Zhao, H. $CsPbBr_3$ perovskite-based heterostructures in photocatalysis: mechanisms, stability, and multifunctional performance. *Adv. Sci.* **2025**, *12*, e07747.

[26] Zhang, D. S.; Wang, L.; Zhang, X. D.; Li, X. B.; Xu, H. X.; Tung, C. H.; Wu, L. Z. Emerging inorganic–organic hybrid photocatalysts for solar-driven overall water splitting: progress and perspectives. *Chem. Soc. Rev.* **2025**, *54*, 9978-10005.

[27] Wang, L. L.; Shao, W.; Hu, Y.; Chen, W.; Qin, X. W.; Lin, C. J.; Cao, C. Y.; Song, W. G. Dual-vacancy-mediated charge separation in $Cd_{0.5}Zn_{0.5}S/NaNbO_3$ S-scheme heterojunction for enhanced photocatalytic hydrogen evolution. *ACS Catal.* **2025**, *15*, 15876-15893.

[28] Wang, X. H.; Wang, X. H.; Huang, J. F.; Li, S. X.; Meng, A. L. Li, Z. J. Interfacial chemical

Just Accepted

bond and internal electric field modulated Z-scheme S_v-$ZnIn_2S_4$/$MoSe_2$ photocatalyst for efficient hydrogen evolution. *Nat. Commun.* **2021**, *12*, 4112.

[29] Hu, T. P.; Dai, K.; Zhang, J. F.; Chen, S. F. Noble-metal-free Ni_2P modified step-scheme $SnNb_2O_6$/CdS-diethylenetriamine for photocatalytic hydrogen production under broadband light irradiation. *Appl. Catal. B Environ.* **2020**, *269*, 118844.

[30] Hu, C.; Tu, S. C.; Tian, N.; Ma, T. Y.; Zhang, Y. H.; Huang, H. W. Photocatalysis enhanced by external fields. *Angew. Chem. Int. Ed.* **2021**, *60*, 16309-16328.

[31] Li, R.; Qiu, L. P.; Cao, S. Z.; Li, Z.; Gao, S. L.; Zhang, J.; Ramakrishna, S.; Long, Y. Z. Research advances in magnetic field-assisted photocatalysis. *Adv. Funct. Mater.* **2024**, *34*, 2316725.

[32] Li, X. B.; Wang, W. W.; Dong, F.; Zhang, Z. Q.; Han, L.; Luo, X. D.; Huang, J. T.; Feng, Z. J.; Chen, Z.; Jia, G. H.; Zhang, T. R. Recent advances in noncontact external-field-assisted photocatalysis: from fundamentals to applications. *ACS Catal.* **2021**, *11*, 4739-4769.

[33] Zhao, X. L.; Gao, W. Q.; Liu, Q. L.; Cui, C.; Zhou, W. J.; Wang, X. N.; Zhang, X. L.; Zhao, L. L.; Sang, Y. H.; Liu, H. Enhanced photo-induced carrier separation of CdS/MoS_2 via micro-potential of Mo microsheet derived from electromagnetic induction. *Chem. Eng. J.* **2021**, *404*, 126972.

[34] Xiao, X. P.; Li, S.; Zuo, L.; Li, R.; Li, Z. W.; Liu, L. J.; Fan, H. T.; Li, B. Twin S-Scheme heterojunction ZnO/UiO-66-NH_2@$ZnIn_2S_4$ rhombic octahedra for efficient photocatalytic H_2 evolution. *Adv. Funct. Mater.* **2025**, *35*, 2418778.

[35] Lu, Y. R.; Dong, Y. B.; Liu, W.; Jin, Q.; Lin, H. Piezo-photocatalytic enhanced microplastic degradation on hetero-interpenetrated $Fe_{1-x}S$/$FeMoO_4$/MoS_2 by producing H_2O_2 and self-Fenton action. *Chem. Eng. J.* **2025**, *508*, 160935.

[36] Wu, C.; Huang, W. X.; Liu, H. M.; Lv, K. L.; Li, Q. Insight into synergistic effect of Ti_3C_2 MXene and MoS_2 on anti-photocorrosion and photocatalytic of CdS for hydrogen production. *App. Catal. B: Environ.* **2023**, *330*, 122653.

[37] Hao, Y. Q.; Yang, H.; Lin, Y. F.; Guo, Q. W.; Hao, X. Q.; Jin, Z. L. Interface ultrafast charge transfer of 1T-MoS_2/ZnCdS QDs Schottky junction for efficient photocatalytic hydrogen evolution. *App. Catal. B: Environ.* **2026**, *382*, 125934.

[38] Yang, R. J.; Fan, Y. Y.; Zhang, Y. F.; Mei, L.; Zhu, R. S.; Qin, J. Q.; Hu, J. H.; Chen, Z. X.; Ng, Y. H.; Voiry, D.; Li, S.; Lu, Q. Y.; Wang, Q.; Yu, J. C.; Zeng, Z. Y. 2D transition metal dichalcogenides for photocatalysis. *Angew. Chem. Int. Ed.* **2023**, *62*, e202218016.

[39] Ma, T. X.; Li, R. Q.; Huang, Y. C.; Lu, Y. X.; Guo, L.; Niu, M. M.; Huang, X.; Soomro, R. A.; Ren, J. Y.; Wang, Q.; Xu, B.; Yang, C. M.; Fu, F.; Wang, D. J. Interfacial chemical-bonded MoS_2/In–Bi_2MoO_6 heterostructure for enhanced photocatalytic nitrogen-to-ammonia conversion. *ACS Catal.* **2024**, *14*, 6292-6304.

[40] Wang, N. N.; Li, C.; Wang, S.; Yuan, Z. X.; Xiao, Y. J.; Li, C.Y.; Liu, C. J.; Chen, S. S.; Zhang, F. X. Synergistic surface modifications enable direct photocatalytic overall water

Just Accepted

splitting over a $MgTa_2O_{6-x}N_y$/TaON heterostructure. *ACS Catal.* **2025**, *15*, 18013-18023.

Just Accepted

Electronic Supplementary Material

Magnetic-field-induced micro-potential promotes charge separation in S-vacancy-rich ZIS/MoS_2/Mo heterostructure for efficient photocatalytic H_2 evolution

Chao Cui[1,✉], Bei Li[2], Liwei Zhu[1], Wencai Zhu[1], Xiaolei Zhao[3], Xiaoning Wang[4], Yuanhua Sang[2], Hong Liu[2], Yan Zhang[1,✉], and Zhaoke Zheng[2,✉]

[1] *School of Chemistry and Chemical Engineering, Shandong Provincial Engineering Research Center for Anti-aging Cosmetics, Qilu Normal University, Jinan 250200, China*

[2] *State Key Laboratory of Crystal Materials, Shandong University, Jinan 250100, China*

[3] *School of Chemistry and Chemical Engineering, Taishan University, Taian 271000, China*

[4] *School of Transportation and Civil Engineering, Shandong Jiaotong University, Jinan 250357, China*

✉Address correspondence to Chao Cui, chaocui_sdu@163.com; Yan Zhang, yanzhang_2003@163.com; Zhaoke Zheng, zkzheng@sdu.edu.cn

Supporting information to https://doi.org/10.26599/NR.2026.94909282

Just Accepted

Experimental

Chemicals and reagents

Anhydrous sodium sulfite (Na_2SO_3, 99.9%), indium trichloride tetrahydrate ($InCl_3 \cdot 4H_2O$, 99.9%), zinc acetate dihydrate ($Zn(CH_3COO)_2 \cdot 2H_2O$, 99.9%), molybdenum trioxide (MoO_3, 99.9%), thioacetamide (TAA, 99.9%) and sodium sulfide nonahydrate ($Na_2S \cdot 9H_2O$, 99.9%) were purchased from Sinopharm Chemical Reagent Co., Ltd. (Shanghai, China). Ultrapure water produced by a UPHW-III-90T

water purification system was used for the preparation of all aqueous solutions throughout the experiments.

Synthesis of metallic Mo sheets

Metallic Mo sheets were synthesized via a temperature-programmed reduction method. MoO_3 powder was placed in the center of a quartz tube. Under an Ar/H_2 mixed atmosphere (10 vol% H_2), the furnace was heated from room temperature to 900 °C at a heating rate of 20 °C/min and maintained at 900 °C for 2 h. Gray Mo sheets were collected from the upper inner wall of the quartz tube, while the by-product MoO_2 remained at the downstream section of the tube.

Synthesis of pure ZIS

$InCl_3 \cdot 4H_2O$ (442 mg, 2 mmol), $Zn(CH_3COO)_2 \cdot 2H_2O$ (220 mg, 1 mmol), and TAA (451 mg, 6 mmol) were were sequentially dissolved in 40 mL of deionized water. The resulting mixture was transferred into a 50 mL Teflon-lined stainless steel autoclave and heated at 200 °C for 24 h. The obtained yellow precipitate was washed repeatedly with deionized water and ethanol, then dried overnight under vacuum at 70 °C.

Synthesis of pure MoS_2

MoO_3 (288 mg, 2 mmol) was uniformly dispersed in a mixed solvent containing 40 mL deionized water and 20 mL ethanol via ultrasonication and magnetic stirring for 30 min, respectively. Subsequently, TAA (451 mg, 6 mmol) was added and fully dissolved in the above suspension. The mixture was transferred into a 100 mL Teflon-lined autoclave and heated at 200 °C for 24 h. The collected precipitate was rinsed thoroughly with deionized water and ethanol, followed by vacuum drying at 70 °C overnight.

Synthesis of the MoS_2/Mo composite

Metallic Mo sheets (192 mg, 2 mmol) were uniformed dispersed in a mixed solution of 40 mL deionized water and 20 mL ethanol via ultrasonication and stirring for 30

Just Accepted

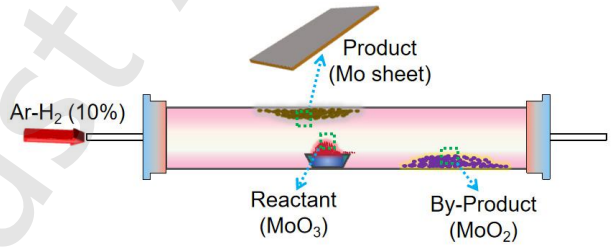
min, respectively. TAA (300.8 mg, 4 mmol) was then dissolved in the suspension. The resultant mixture was transferred to a 100 mL Teflon-lined autoclave and reacted at 200 °C for 24 h. The solid product was washed several times with deionized water and ethanol, and finally dried under vacuum at 70 °C overnight.

Synthesis of the ZIS/MoS_2 heterostructure

$InCl_3 \cdot 4H_2O$ (1173 mg, 4 mmol), $Zn(CH_3COO)_2 \cdot 2H_2O$ (439 mg, 2 mmol) and TAA (902 mg, 12 mmol) were sequentially dissolved in a mixed solvent of 40 mL deionized water and 20 mL ethanol. MoO_3 (288 mg, 2 mmol) was then homogeneously dispersed into the above solution. The mixture was sealed in a 100 mL Teflon-lined autoclave and heated at 200 °C for 24 h. The black precipitate was collected, washed with deionized water and ethanol, and dried under vacuum at 70 °C overnight.

Synthesis of pure ZIS_v, pure MoS_{2-x}, and the ZIS_v/MoS_{2-x} heterostructure

ZIS_v, MoS_{2-x}, and ZIS_v/MoS_{2-x} were prepared following the same hydrothermal and post-treatment procedures as ZIS_v/MoS_{2-x}/Mo, except that the precursor ZIS/MoS_2/Mo was replaced with pure ZIS, pure MoS_2 and the ZIS/MoS_2 heterostructure, respectively.



Scheme S1 Schematic illustration for the synthesis of metallic Mo sheets.

Just Accepted

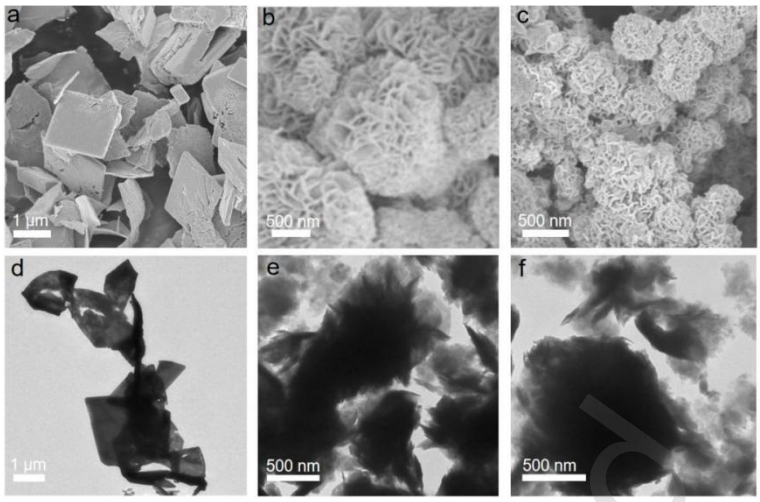


Figure S1 SEM images of (a) metallic Mo sheets, (b) pure ZIS and (c) ZIS_v . TEM images of (d) metallic Mo sheets, (e) pure ZIS and (f) ZIS_v.

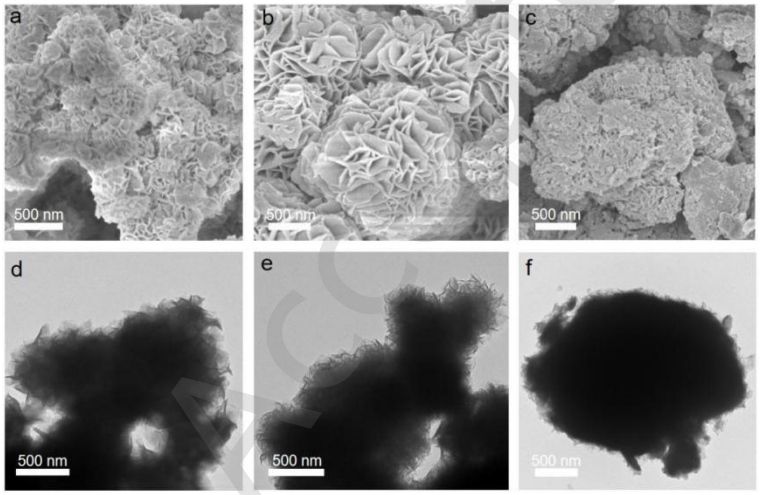


Figure S2 SEM images of (a) the ZIS/MoS_2, (b) ZIS_v/MoS_{2-x} and (c) $ZIS/MoS_2/Mo$ heterostructures. TEM images of (d) the ZIS/MoS_2, (e) ZIS_v/MoS_{2-x} and (f) $ZIS/MoS_2/Mo$ heterostructures.

Just Accepted

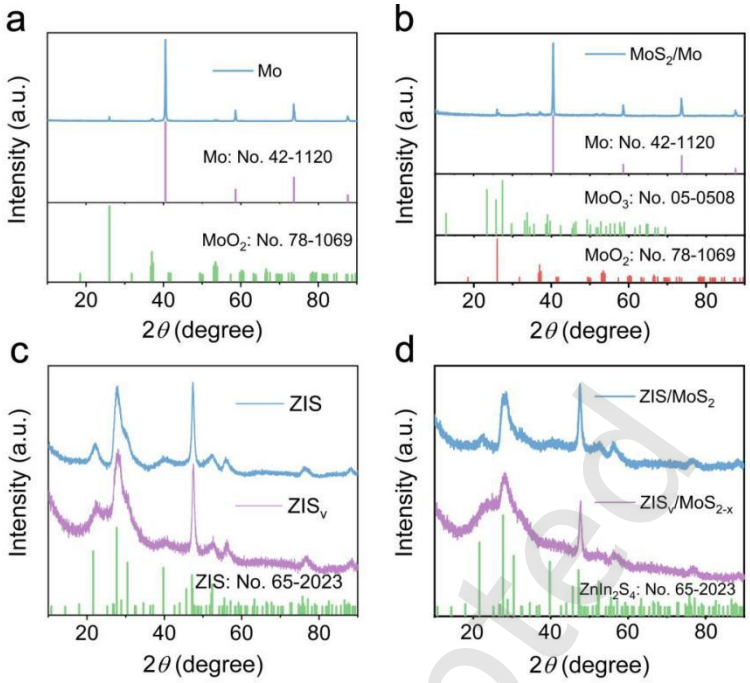


Figure S3 XRD patterns of (a) metallic Mo sheets, (b) MoS_2/Mo composite,(c) pure ZIS and ZIS_v, (d) the ZIS/MoS_2 and ZIS_v/MoS_{2-x} heterostructures.

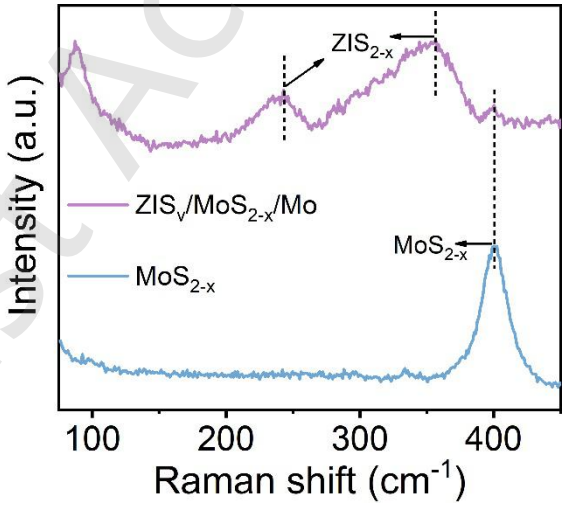


Figure S4 Raman spectra of pure MoS_{2-x} and the ZIS_v/MoS_{2-x}/Mo heterostructure.

Just Accepted

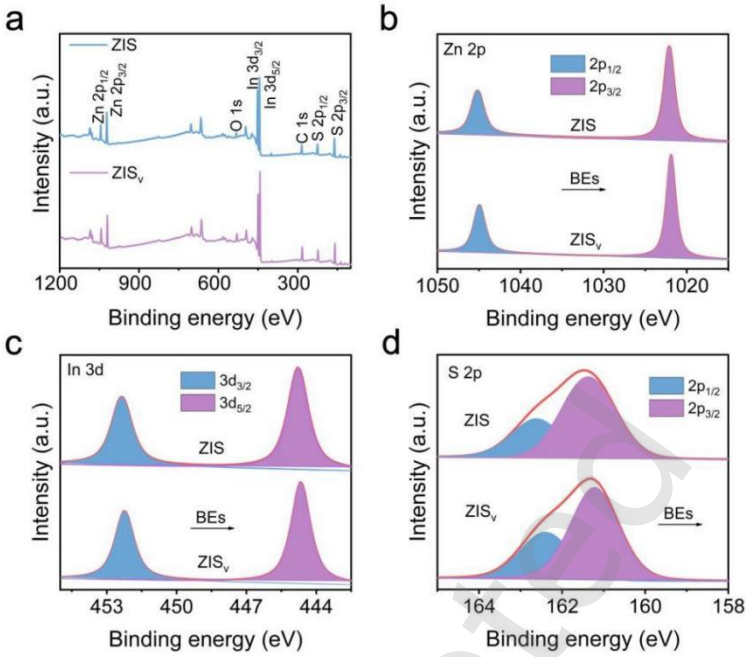


Figure S5 (a) XPS survey spectra of pure ZIS and ZIS_v. High-resolution XPS spectra of (b) Zn 2p, (c) In 3d, and (d) S 2p for pure ZIS and ZIS_v.

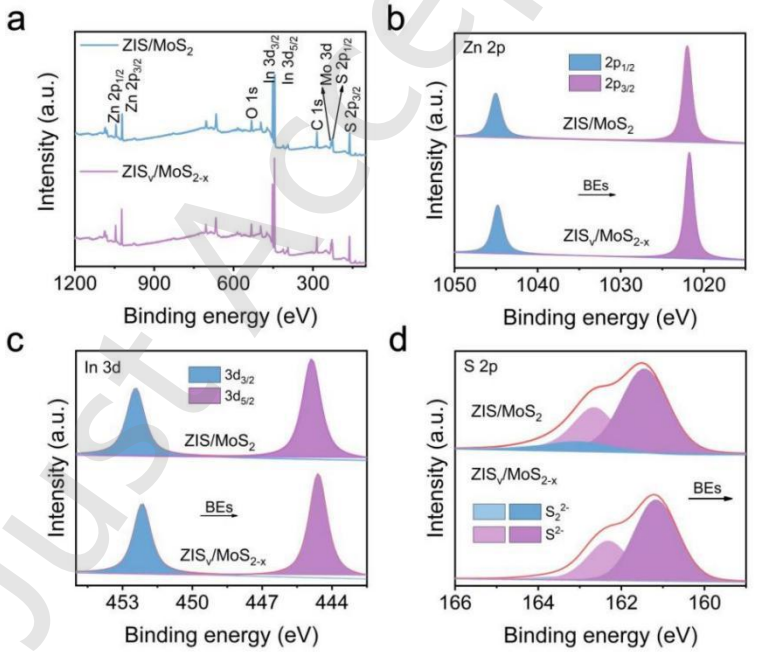


Figure S6 (a) XPS survey spectra of the ZIS/MoS_2 and ZIS_v/MoS_{2-x} heterostructures. High-resolution XPS spectra of (b) Zn 2p, (c) In 3d, and (d) S 2p for the ZIS/MoS_2 and ZIS_v/MoS_{2-x} heterostructures.

Just Accepted

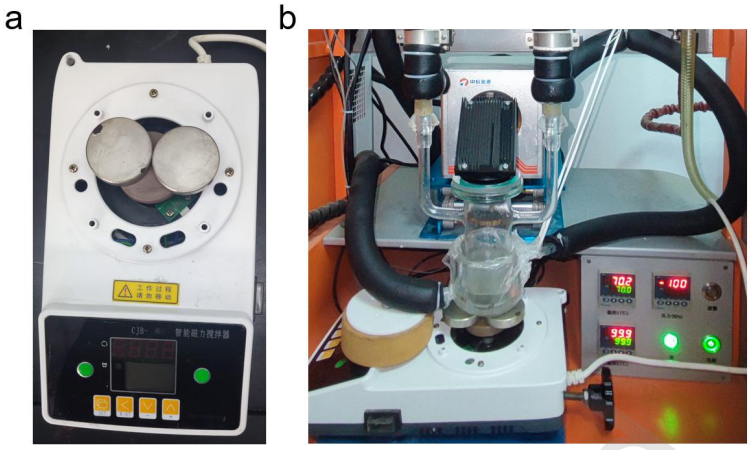


Figure S7 (a) Digital photograph of the magnetic-field-coupled magnetic stirrer. (b) Photograph of the overall setup for magnetic field-assisted PHE reaction.

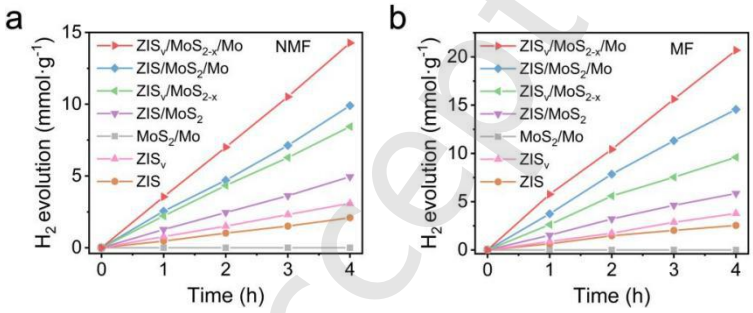


Figure S8 Time-dependent H_2 evolution profiles of various photocatalysts under (a) NMF and (b) MF conditions.

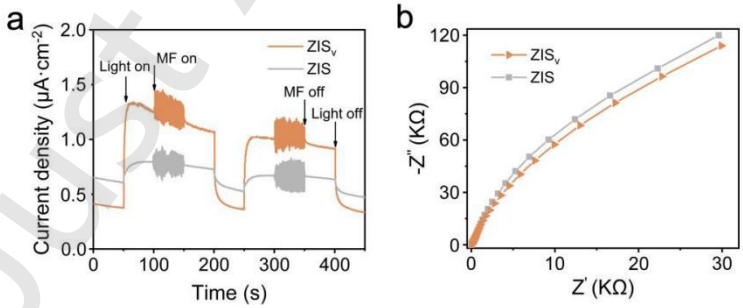


Figure S9 (a) I-t curves of pure ZIS and ZIS_V under light irradiation and MF conditions. (b) EIS curves of pure ZIS and ZIS_V.

Just Accepted

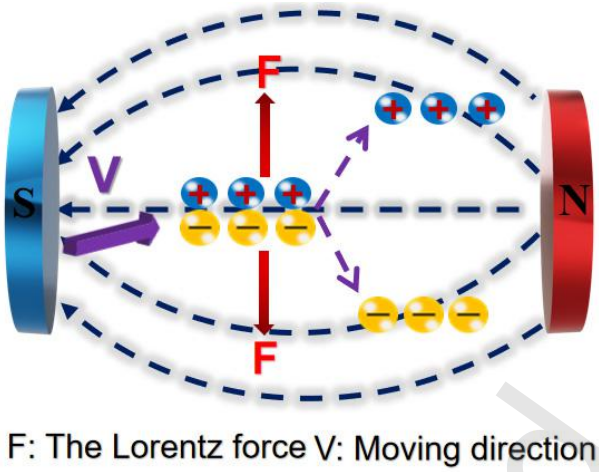


Figure S10 Schematic diagram illustrating the Lorentz force that drives photogenerated electrons and holes to migrate in opposite directions.

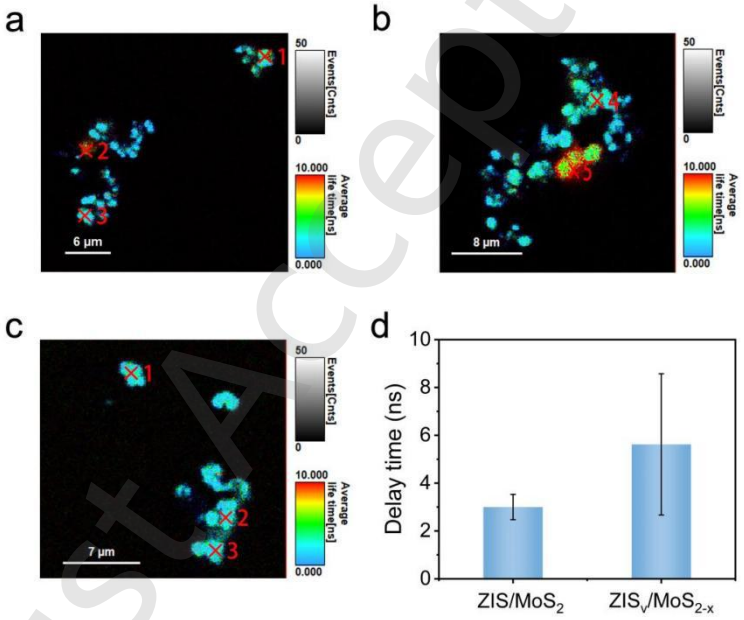


Figure S11 Single-particle PL mapping images of (a, b) the ZIS_v/MoS_{2-x} and (c) ZIS/MoS_2 heterostructures. (d) Time-resolved PL spectra of the ZIS/MoS_2 and ZIS_v/MoS_{2-x} heterostructures.

Just Accepted

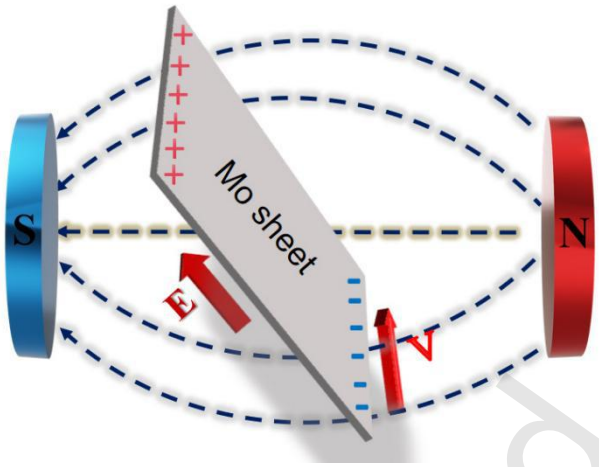


Figure S12 Schematic diagram of the magnetic-field-induced micro-potential parallel to metallic Mo sheet and the induced electric field.

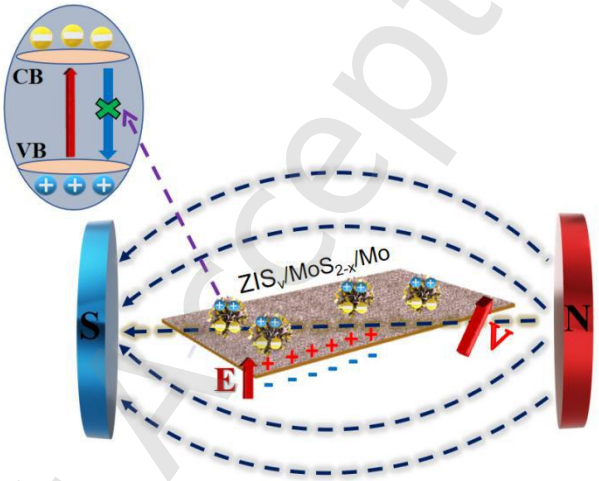


Figure S13 Schematic diagram of the micro-potential perpendicular to metallic Mo sheet and the induced electric field for accelerating the separation of photo-induced charge carriers.

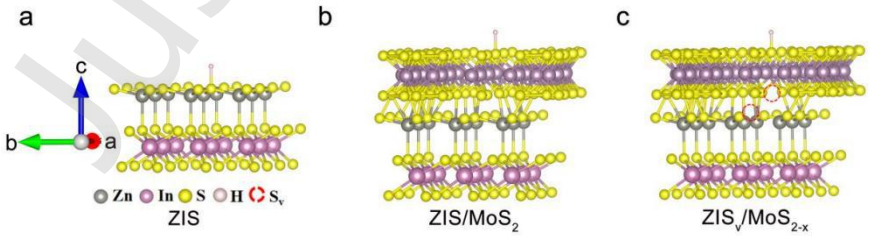


Figure S14 Optimized geometric models for single H atom adsorption on the surface of (a) pure ZIS, (b) the ZIS/MoS_2, and (c) ZIS_v/MoS_{2-x} heterostructures.

Just Accepted

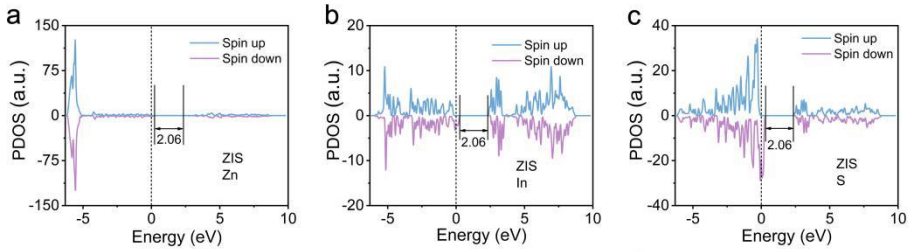


Figure S15 PDOS of (a) Zn, (b) In, and (c) S elements in pure ZIS.

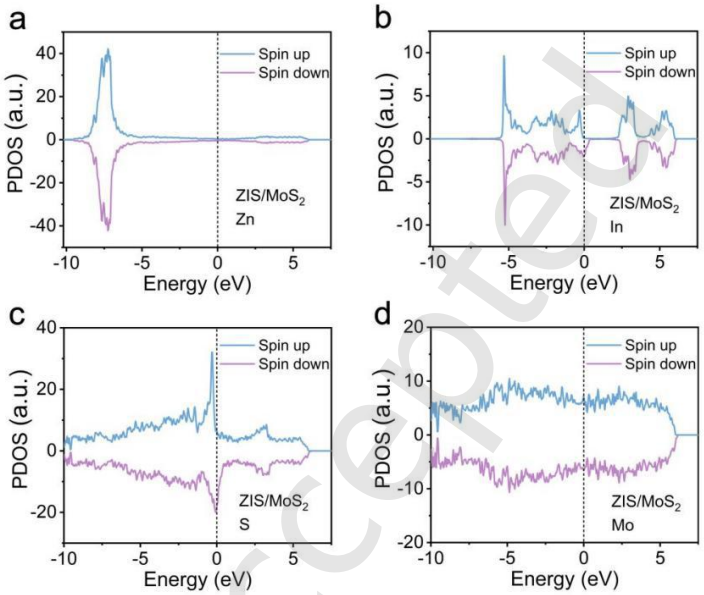


Figure S16 PDOS of (a) Zn, (b) In, (c) S and (d) Mo elements in the ZIS/MoS_2 heterostructure.

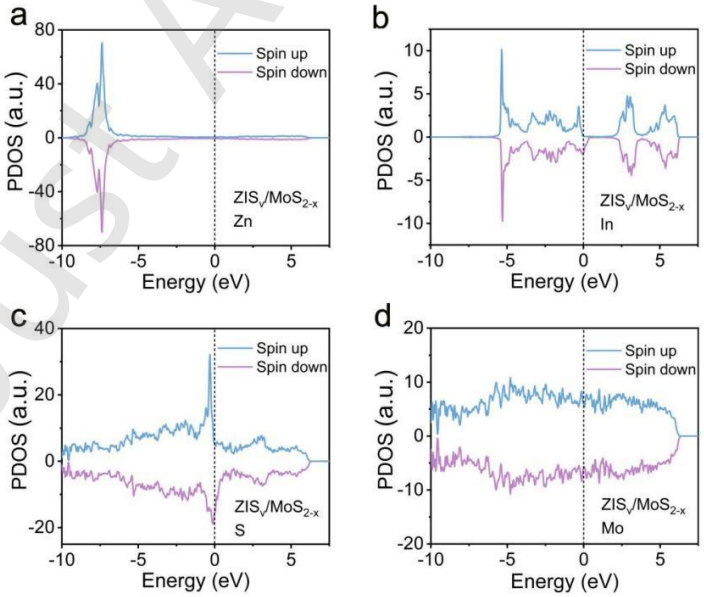


Figure S17 PDOS of (a) Zn, (b) In, (c) S and (d) Mo elements in the ZIS_v/MoS_{2-x} heterostructure.

Just Accepted

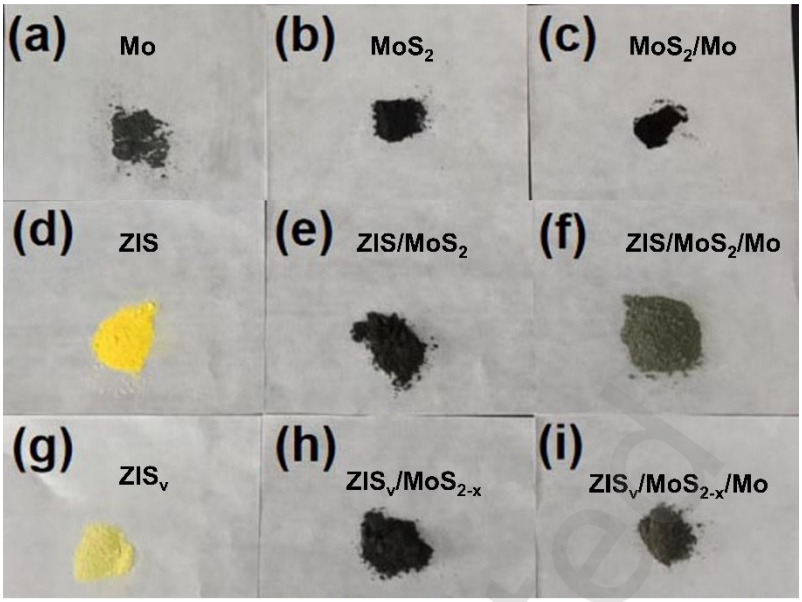


Figure S18 Digital photographs of as-prepared powder samples: (a) metallic Mo sheets, (b) pure MoS_2, (c) MoS_2/Mo composite, (d) pure ZIS, (e) the ZIS/MoS_2 heterostructures, (f) the ZIS/MoS_2/Mo heterostructures, (g) ZIS_v, (h) the ZIS_v/MoS_{2-x}, and (i) ZIS_v/MoS_{2-x}/Mo heterostructures.

Table S1 Calculated AQY of the ZIS_v/MoS_{2-x}/Mo heterostructure at different monochromatic wavelengths

Wavelength (nm)	**The mean H_2 evolution in 1 hour (μmol)**	**Light power (W)**
380	9.67	0.016
420	18.26	0.165

The AQY measurements were performed under the same reaction conditions as the photocatalytic tests. Monochromatic light was obtained by equipping a 300 W xenon lamp with corresponding band-pass filters (λ = 380 nm and 420 nm). The AQY values were calculated according to the following equations:

Just Accepted

$$AQY = \frac{\text{the number of reacted electrons}}{\text{the number of produced photons}} \times 100\%$$
$$= \frac{4 \times \text{the number of } H_2 \text{ molecules}}{\text{the number of produced photons}} \times 100\%$$
$$= \frac{4 \times \text{the number of } H_2 \text{ molecules}}{N} \times 100\%$$

λ =380 nm:

$$N = \frac{E\lambda}{hc} = \frac{0.016 \times 3600 \times 380 \times 10^{-9}}{6.626 \times 10^{-34} \times 3 \times 10^{8}} = 1.11 \times 10^{20}$$

$$AQY = \frac{4 \times 9.67 \times 10^{-6} \times 6.02 \times 10^{23}}{1.11 \times 10^{20}} \times 100\% = 20.98\%$$

λ =420 nm:

$$N = \frac{E\lambda}{hc} = \frac{0.165 \times 3600 \times 420 \times 10^{-9}}{6.626 \times 10^{-34} \times 3 \times 10^{8}} = 1.26 \times 10^{21}$$

$$AQY = \frac{4 \times 18.26 \times 10^{-6} \times 6.02 \times 10^{23}}{1.26 \times 10^{21}} \times 100\% = 3.49\%$$

Table S2 Bader charge analysis of the ZIS/MoS_2 heterostructure

Atom	x	y	z	Actual charge
Zn1	5.899719	10.143646	5.942163	11.245192
Zn2	-1.946998	10.135458	5.959093	11.177924
Zn3	1.991617	10.146032	5.959212	11.1933
Zn4	9.826395	3.34069	5.979361	11.162777
Zn5	1.976316	3.361267	5.989654	11.174546
Zn6	5.918564	3.347603	5.990409	11.168161
Zn7	7.865285	6.724033	5.951542	11.179492
Zn8	0.032309	6.720331	5.971373	11.157109
Zn9	3.969817	6.742571	5.96108	11.149265

Just Accepted

In1	0.020717	2.211502	2.043909	1.84794
In2	3.944102	2.213072	2.043671	1.845689
In3	7.867652	2.210115	2.044227	1.847348
In4	-1.942153	5.612495	2.045379	1.846894
In5	1.982892	5.612087	2.04689	1.843147
In6	5.904529	5.612465	2.046532	1.84479
In7	-3.906065	9.006178	2.043631	1.846102
In8	0.020935	9.006545	2.044108	1.845726
In9	3.943602	9.005097	2.045658	1.846214
S1	0.033233	2.238992	6.450289	6.363561
S2	1.982203	1.077398	0.547231	6.612597
S3	5.907661	10.141943	3.385082	6.783619
S4	3.948447	2.212705	6.468133	6.803177
S5	5.906466	1.077796	0.547112	6.61323
S6	-1.943607	10.141046	3.389453	6.803493
S7	7.878161	2.214652	6.461377	6.41816
S8	9.831311	1.078102	0.548661	6.613637
S9	1.981103	10.140893	3.384485	6.815132
S10	-1.936354	5.624966	6.470796	6.55147
S11	0.019698	4.476557	0.546555	6.60603
S12	9.831682	3.343484	3.382379	6.792276
S13	3.944149	4.476649	0.545323	6.610385
S14	1.982515	3.341149	3.38373	6.814663
S15	5.901597	5.612873	6.471908	6.519981
S16	7.868859	4.476231	0.547986	6.606666
S17	5.905118	3.342199	3.383333	6.811992
S18	-3.904911	9.004363	6.358965	6.383059
S19	-1.943101	7.876715	0.545164	6.613025
S20	7.869642	6.74359	3.380869	6.801089

Just Accepted

S21	0.054191	9.003986	6.398984	6.425419
S22	1.981391	7.875919	0.544171	6.613985
S23	0.01795	6.743386	3.382737	6.814828
S24	3.956848	9.010583	6.437095	6.295194
S25	5.907208	7.876847	0.544489	6.615052
S26	3.945862	6.744783	3.378206	6.794282
S27	-3.081393	8.472638	7.974031	6.236207
S28	-3.105413	8.488811	12.035064	6.227756
S29	-0.095607	8.388984	8.013057	6.126767
S30	-0.080666	8.387536	11.986381	6.257671
S31	3.077284	8.369997	7.978283	6.242584
S32	3.123586	8.386546	11.981334	6.218044
S33	6.056559	8.193428	7.706138	6.318403
S34	6.07568	8.210355	12.19208	6.218063
S35	0.869738	1.694726	7.966242	6.290102
S36	0.855503	1.754071	12.024731	6.361003
S37	3.88513	1.654479	8.043935	5.859534
S38	3.881604	1.67578	11.964842	6.412287
S39	7.034697	1.656192	8.018938	6.326977
S40	7.06498	1.655661	11.965994	6.397004
S41	10.006106	1.539703	7.736063	6.450255
S42	10.018334	1.552214	12.188543	6.302099
S43	-0.883767	4.029181	8.395999	6.428368
S44	-0.878957	4.037103	11.550465	6.372738
S45	2.234768	4.017505	11.528249	6.500352
S46	5.41835	4.010163	8.416903	6.587353
S47	5.419192	4.016129	11.536078	6.483263
S48	8.438918	3.871384	8.178895	6.524894
S49	8.441302	3.861463	11.773848	6.429157

Just Accepted

S50	-2.339047	6.516252	8.346839	6.322658
S51	-2.330169	6.479727	11.606817	6.384117
S52	0.766931	6.477545	8.328281	6.503667
S53	0.783003	6.451053	11.608923	6.473449
S54	3.968816	6.468418	8.355582	6.460303
S55	3.976617	6.434473	11.616752	6.377073
S56	6.936723	6.247687	8.098181	6.381655
S57	6.944853	6.25559	11.854203	6.39414
S58	-4.03361	10.137508	7.945855	6.2357
S59	-4.040245	10.103277	12.057239	6.154432
S60	-0.988135	10.012362	7.958691	6.343538
S61	-0.994092	10.008242	12.005536	6.216101
S62	2.216377	10.000054	7.938741	6.30275
S63	2.19838	10.009017	12.010464	6.160846
S64	5.11123	9.840902	7.640328	6.187862
S65	5.11359	9.831245	12.296757	6.217598
S66	2.067284	3.78621	8.41424	6.576473
S67	2.10541	5.630737	6.476439	6.675838
Mo1	-4.880424	9.233914	10.001805	5.476975
Mo2	-2.126851	8.844109	9.968304	5.478113
Mo3	1.085638	8.793961	9.937783	5.435757
Mo4	3.987049	8.67215	9.947678	5.510359
Mo5	-0.711639	2.962754	9.957852	5.390841
Mo6	2.018174	2.451912	10.012615	5.282279
Mo7	5.199696	2.47304	9.949347	5.267875
Mo8	8.274213	2.487397	9.959203	5.332049
Mo9	-2.167672	5.154606	9.95209	5.219395
Mo10	0.676116	4.88231	9.947162	5.147065
Mo11	3.802457	4.876936	9.937266	5.135818
Mo12	6.815112	4.859989	9.955507	5.175967

Just Accepted

Mo13	-3.911052	7.367474	9.96433	5.384383
Mo14	-1.135384	7.171297	9.966873	5.368458
Mo15	2.028735	7.191099	9.969218	5.36186
Mo16	4.933591	6.962639	9.950103	5.396401
Mo17	0.15286	0.877714	9.961071	5.479626
Mo18	2.726857	0.544573	9.946446	5.483967
Mo19	5.858809	0.602837	9.949069	5.472833
Mo20	8.750789	0.358052	9.956541	5.543286
Sum of the electrons: 657				
Number of electrons transport		Semiconductor	Original charge	Actual charge
-0.62 e$^-$		ZIS	297	296.38
+0.60 e$^-$		MoS_2	360	360.60

The actual charge of Zn, In and S elements from ZIS is marked in red, while that of Mo and S elements from MoS_2 is marked in green.

Table S3 Bader charge analysis of the ZIS_v/MoS_{2-x} heterostructure

Atom	x	y	z	Actual charge
Zn1	-5.858833	10.150855	5.239427	11.212475
Zn2	-1.934105	10.150855	5.239427	11.230533
Zn3	1.990622	10.150855	5.239427	11.221075
Zn4	-1.934105	3.353028	5.239427	11.169297
Zn5	1.990622	3.353028	5.239427	11.309204
Zn6	5.915349	3.353028	5.239427	11.169692
Zn7	-3.896469	6.751942	5.239427	11.182069
Zn8	0.028258	6.751942	5.239427	11.258888
Zn9	3.952986	6.751942	5.239427	11.253595
In1	0.019486	2.210981	2.082815	1.864791
In2	3.944214	2.210981	2.082815	1.861071
In3	7.868941	2.210981	2.082815	1.858553

Just Accepted

In4	-1.942936	5.609997	2.082815	1.860268
In5	1.981791	5.609997	2.082815	1.858582
In6	5.906519	5.609997	2.082815	1.852307
In7	-3.9053	9.008911	2.082815	1.85485
In8	0.019428	9.008911	2.082815	1.85761
In9	3.944155	9.008911	2.082815	1.857056
S1	0.028317	2.219955	5.741353	6.533446
S2	1.98185	1.07801	0.533719	6.621438
S3	5.906636	10.141882	3.337432	6.720965
S4	3.953045	2.219955	5.741353	6.520984
S5	5.906578	1.07801	0.533719	6.636682
S6	-1.942936	10.141882	3.337432	6.735882
S7	7.877772	2.219955	5.741353	6.564023
S8	9.831305	1.07801	0.533719	6.131079
S9	1.981791	10.141882	3.337432	6.235949
S10	-1.934105	5.61897	5.741353	6.627746
S11	0.019428	4.477026	0.533719	6.632244
S12	9.831364	3.344055	3.337432	6.697479
S13	3.944155	4.477026	0.533719	6.636638
S14	1.981791	3.344055	3.337432	6.718316
S15	5.915349	5.61897	5.741353	6.69663
S16	7.868882	4.477026	0.533719	6.630079
S17	5.906519	3.344055	3.337432	6.723562
S18	-3.896469	9.017884	5.741353	6.388669
S19	-1.942936	7.87594	0.533719	6.635283
S20	7.869	6.742968	3.337432	6.719896
S21	0.028258	9.017884	5.741353	6.5438
S22	1.981791	7.87594	0.533719	6.641026
S23	0.019428	6.742968	3.337432	6.723401

Just Accepted

S24	3.952986	9.017884	5.741353	6.671487
S25	5.906519	7.87594	0.533719	6.634187
S26	3.944155	6.742968	3.337432	6.72154
S27	-3.644558	8.677819	7.586916	5.537527
S28	-3.644558	8.677819	10.714914	6.321951
S29	-0.45231	8.677819	7.586916	6.027588
S30	-0.45231	8.677819	10.714914	5.987391
S31	2.739938	8.677819	7.586916	6.489645
S32	2.739938	8.677819	10.714914	6.088727
S33	5.932187	8.677819	7.586916	6.134108
S34	5.932187	8.677819	10.714914	5.992201
S35	0.646468	1.245544	7.586916	6.363265
S36	0.646468	1.245544	10.714914	6.37969
S37	3.838716	1.245544	7.586916	6.383934
S38	3.838716	1.245544	10.714914	6.473651
S39	7.030964	1.245544	7.586916	6.383389
S40	7.030964	1.245544	10.714914	6.485589
S41	10.223213	1.245544	7.586916	6.395744
S42	10.223213	1.245544	10.714914	6.350898
S43	-0.949656	4.010112	7.586916	6.562331
S44	-0.949656	4.010112	10.714914	6.473529
S45	2.242592	4.010112	10.714914	6.608367
S46	5.43484	4.010112	7.586916	6.620556
S47	5.43484	4.010112	10.714914	6.560757
S48	8.627088	4.010112	7.586916	6.425549
S49	8.627088	4.010112	10.714914	6.377623
S50	-2.54578	6.774681	7.586916	6.401455
S51	-2.54578	6.774681	10.714914	6.440719
S52	0.646468	6.774681	7.586916	6.636632

Just Accepted

S53	0.646468	6.774681	10.714914	6.466278
S54	3.838716	6.774681	7.586916	6.586913
S55	3.838716	6.774681	10.714914	6.474453
S56	7.030964	6.774681	7.586916	6.295575
S57	7.030964	6.774681	10.714914	6.295492
S58	-4.141904	9.539249	7.586916	6.792324
S59	-4.141904	9.539249	10.714914	5.791965
S60	-0.949656	9.539249	7.586916	6.211252
S61	-0.949656	9.539249	10.714914	6.108593
S62	2.242592	9.539249	7.586916	5.699859
S63	2.242592	9.539249	10.714914	6.020529
S64	5.43484	9.539249	7.586916	6.045131
S65	5.43484	9.539249	10.714914	6.145642
Mo1	-5.240682	9.59941	9.150716	5.68266
Mo2	-2.048434	9.59941	9.150716	5.781132
Mo3	1.143814	9.59941	9.150716	5.782212
Mo4	4.335945	9.59941	9.150716	5.768504
Mo5	-0.949656	2.167135	9.150716	5.279321
Mo6	2.242592	2.167135	9.150716	5.775688
Mo7	5.43484	2.167135	9.150716	5.606726
Mo8	8.626971	2.167135	9.150716	5.203903
Mo9	-2.54578	4.931703	9.150716	5.163361
Mo10	0.646468	4.931703	9.150716	5.166457
Mo11	3.838716	4.931703	9.150716	5.122241
Mo12	7.030847	4.931703	9.150716	5.188493
Mo13	-4.141904	7.696271	9.150716	5.453711
Mo14	-0.949656	7.696271	9.150716	5.336342
Mo15	2.242592	7.696271	9.150716	5.299331
Mo16	5.434723	7.696271	9.150716	5.400731
Mo17	0.149122	0.263996	9.150716	5.736984

Just Accepted

Mo18	3.34137	0.263996	9.150716	5.630349
Mo19	6.533618	0.263996	9.150716	5.624084
Mo20	9.725748	0.263996	9.150716	5.686605
Sum of the electrons: 645				
Number of electrons transport		Semiconductor	Original charge	Actual charge
-1.53 e$^-$		ZIS_v	291	289.47
+1.52 e$^-$		MoS_{2-x}	354	355.52

The actual charge of Zn, In and S elements from ZIS_v is marked in red, while that of Mo and S elements from MoS_{2-x} is marked in green.

Table S4 Atomistic coordinates for the Pawley-refined ZIS/MoS_2 heterostructure

Lattice type: P			
Space group: P1			
a=11.7743, b=11.7743, c=39.7408, α=90°, β=90°, γ=120°			
Unit-cell volume =4771.307337 Å^3			
Structure parameters			
Atom	x	y	z
Zn1	0.99896	0.99461	0.15197
Zn2	0.33229	0.99461	0.15197
Zn3	0.66562	0.99461	0.15197
Zn4	0.99896	0.32795	0.15197
Zn5	0.33229	0.32795	0.15197
Zn6	0.66562	0.32795	0.15197
Zn7	0.99896	0.66128	0.15197
Zn8	0.33229	0.66128	0.15197
Zn9	0.66562	0.66128	0.15197
In1	0.11007	0.21683	0.05241
In2	0.4434	0.21683	0.05241
In3	0.77673	0.21683	0.05241
In4	0.11007	0.55017	0.05241

Just Accepted

In5	0.4434	0.55017	0.05241
In6	0.77673	0.55017	0.05241
In7	0.11007	0.8835	0.05241
In8	0.4434	0.8835	0.05241
In9	0.77673	0.8835	0.05241
S1	0.11007	0.21683	0.1646
S2	0.22118	0.10572	0.01343
S3	0.99896	0.99461	0.08398
S4	0.4434	0.21683	0.1646
S5	0.55451	0.10572	0.01343
S6	0.33229	0.99461	0.08398
S7	0.77673	0.21683	0.1646
S8	0.88784	0.10572	0.01343
S9	0.66562	0.99461	0.08398
S10	0.11007	0.55017	0.1646
S11	0.22118	0.43906	0.01343
S12	0.99896	0.32795	0.08398
S13	0.55451	0.43906	0.01343
S14	0.33229	0.32795	0.08398
S15	0.77673	0.55017	0.1646
S16	0.88784	0.43906	0.01343
S17	0.66562	0.32795	0.08398
S18	0.11007	0.8835	0.1646
S19	0.22118	0.77239	0.01343
S20	0.99896	0.66128	0.08398
S21	0.4434	0.8835	0.1646
S22	0.55451	0.77239	0.01343
S23	0.33229	0.66128	0.08398
S24	0.77673	0.8835	0.1646

Just Accepted

S25	0.88784	0.77239	0.01343
S26	0.66562	0.66128	0.08398
S27	0.11479	0.85015	0.21104
S28	0.11479	0.85015	0.28975
S29	0.38591	0.85015	0.21104
S30	0.38591	0.85015	0.28975
S31	0.65703	0.85015	0.21104
S32	0.65703	0.85015	0.28975
S33	0.92815	0.85015	0.21104
S34	0.92815	0.85015	0.28975
S35	0.11479	0.12127	0.21104
S36	0.11479	0.12127	0.28975
S37	0.38591	0.12127	0.21104
S38	0.38591	0.12127	0.28975
S39	0.65703	0.12127	0.21104
S40	0.65703	0.12127	0.28975
S41	0.92815	0.12127	0.21104
S42	0.92815	0.12127	0.28975
S43	0.11479	0.39239	0.21104
S44	0.11479	0.39239	0.28975
S45	0.38591	0.39239	0.28975
S46	0.65703	0.39239	0.21104
S47	0.65703	0.39239	0.28975
S48	0.92815	0.39239	0.21104
S49	0.92815	0.39239	0.28975
S50	0.11479	0.66351	0.21104
S51	0.11479	0.66351	0.28975
S52	0.38591	0.66351	0.21104
S53	0.38591	0.66351	0.28975

Just Accepted

S54	0.65703	0.66351	0.21104
S55	0.65703	0.66351	0.28975
S56	0.92815	0.66351	0.21104
S57	0.92815	0.66351	0.28975
S58	0.11479	0.93463	0.21104
S59	0.11479	0.93463	0.28975
S60	0.38591	0.93463	0.21104
S61	0.38591	0.93463	0.28975
S62	0.65703	0.93463	0.21104
S63	0.65703	0.93463	0.28975
S64	0.92815	0.93463	0.21104
S65	0.92815	0.93463	0.28975
S66	0.35362	0.35957	0.2124
S67	0.45942	0.5547	0.16415
Mo1	0.02442	0.94053	0.25039
Mo2	0.29554	0.94053	0.25039
Mo3	0.56666	0.94053	0.25039
Mo4	0.83777	0.94053	0.25039
Mo5	0.02442	0.21165	0.25039
Mo6	0.29554	0.21165	0.25039
Mo7	0.56666	0.21165	0.25039
Mo8	0.83777	0.21165	0.25039
Mo9	0.02442	0.48277	0.25039
Mo10	0.29554	0.48277	0.25039
Mo11	0.56666	0.48277	0.25039
Mo12	0.83777	0.48277	0.25039
Mo13	0.02442	0.75389	0.25039
Mo14	0.29554	0.75389	0.25039
Mo15	0.56666	0.75389	0.25039
Mo16	0.83777	0.75389	0.25039

Just Accepted

Mo17	0.02442	0.02501	0.25039
Mo18	0.29554	0.02501	0.25039
Mo19	0.56666	0.02501	0.25039
Mo20	0.83777	0.02501	0.25039

Table S5 Atomistic coordinates for the Pawley-refined ZIS_v/MoS_{2-x} heterostructure

Lattice type: P			
Space group: P1			
a=11.7743, b=11.7743, c=39.7408, α=90°, β=90°, γ=120°			
Unit-cell volume =4771.307337 Å^3			
Structure parameters			
Atom	x	y	z
Zn1	0.99896	0.99461	0.15197
Zn2	0.33229	0.99461	0.15197
Zn3	0.66562	0.99461	0.15197
Zn4	0.99896	0.32795	0.15197
Zn5	0.33229	0.32795	0.15197
Zn6	0.66562	0.32795	0.15197
Zn7	0.99896	0.66128	0.15197
Zn8	0.33229	0.66128	0.15197
Zn9	0.66562	0.66128	0.15197
In1	0.11007	0.21683	0.05241
In2	0.4434	0.21683	0.05241
In3	0.77673	0.21683	0.05241
In4	0.11007	0.55017	0.05241
In5	0.4434	0.55017	0.05241
In6	0.77673	0.55017	0.05241
In7	0.11007	0.8835	0.05241
In8	0.4434	0.8835	0.05241
In9	0.77673	0.8835	0.05241

Just Accepted

S1	0.11007	0.21683	0.1646
S2	0.22118	0.10572	0.01343
S3	0.99896	0.99461	0.08398
S4	0.4434	0.21683	0.1646
S5	0.55451	0.10572	0.01343
S6	0.33229	0.99461	0.08398
S7	0.77673	0.21683	0.1646
S8	0.88784	0.10572	0.01343
S9	0.66562	0.99461	0.08398
S10	0.11007	0.55017	0.1646
S11	0.22118	0.43906	0.01343
S12	0.99896	0.32795	0.08398
S13	0.55451	0.43906	0.01343
S14	0.33229	0.32795	0.08398
S15	0.77673	0.55017	0.1646
S16	0.88784	0.43906	0.01343
S17	0.66562	0.32795	0.08398
S18	0.11007	0.8835	0.1646
S19	0.22118	0.77239	0.01343
S20	0.99896	0.66128	0.08398
S21	0.4434	0.8835	0.1646
S22	0.55451	0.77239	0.01343
S23	0.33229	0.66128	0.08398
S24	0.77673	0.8835	0.1646
S25	0.88784	0.77239	0.01343
S26	0.66562	0.66128	0.08398
S27	0.11479	0.85015	0.21104
S28	0.11479	0.85015	0.28975
S29	0.38591	0.85015	0.21104

Just Accepted

S30	0.38591	0.85015	0.28975
S31	0.65703	0.85015	0.21104
S32	0.65703	0.85015	0.28975
S33	0.92815	0.85015	0.21104
S34	0.92815	0.85015	0.28975
S35	0.11479	0.12127	0.21104
S36	0.11479	0.12127	0.28975
S37	0.38591	0.12127	0.21104
S38	0.38591	0.12127	0.28975
S39	0.65703	0.12127	0.21104
S40	0.65703	0.12127	0.28975
S41	0.92815	0.12127	0.21104
S42	0.92815	0.12127	0.28975
S43	0.11479	0.39239	0.21104
S44	0.11479	0.39239	0.28975
S45	0.38591	0.39239	0.28975
S46	0.65703	0.39239	0.21104
S47	0.65703	0.39239	0.28975
S48	0.92815	0.39239	0.21104
S49	0.92815	0.39239	0.28975
S50	0.11479	0.66351	0.21104
S51	0.11479	0.66351	0.28975
S52	0.38591	0.66351	0.21104
S53	0.38591	0.66351	0.28975
S54	0.65703	0.66351	0.21104
S55	0.65703	0.66351	0.28975
S56	0.92815	0.66351	0.21104
S57	0.92815	0.66351	0.28975
S58	0.11479	0.93463	0.21104

Just Accepted

S59	0.11479	0.93463	0.28975
S60	0.38591	0.93463	0.21104
S61	0.38591	0.93463	0.28975
S62	0.65703	0.93463	0.21104
S63	0.65703	0.93463	0.28975
S64	0.92815	0.93463	0.21104
S65	0.92815	0.93463	0.28975
Mo1	0.02442	0.94053	0.25039
Mo2	0.29554	0.94053	0.25039
Mo3	0.56666	0.94053	0.25039
Mo4	0.83777	0.94053	0.25039
Mo5	0.02442	0.21165	0.25039
Mo6	0.29554	0.21165	0.25039
Mo7	0.56666	0.21165	0.25039
Mo8	0.83777	0.21165	0.25039
Mo9	0.02442	0.48277	0.25039
Mo10	0.29554	0.48277	0.25039
Mo11	0.56666	0.48277	0.25039
Mo12	0.83777	0.48277	0.25039
Mo13	0.02442	0.75389	0.25039
Mo14	0.29554	0.75389	0.25039
Mo15	0.56666	0.75389	0.25039
Mo16	0.83777	0.75389	0.25039
Mo17	0.02442	0.02501	0.25039
Mo18	0.29554	0.02501	0.25039
Mo19	0.56666	0.02501	0.25039
Mo20	0.83777	0.02501	0.25039

Just Accepted